

FAST Pulsar Database: II. Scattering profiles of 122 Pulsars

W. C. JING ,^{1,2} J. L. HAN ,^{1,2,3,*} C. WANG ,^{1,2,3} P. F. WANG ,^{1,2,3} T. WANG ,¹ N. N. CAI ,¹ J. XU ,^{1,3}
Z. L. YANG ,^{1,2} D. J. ZHOU ,¹ YI YAN ,¹ W. Q. SU ,^{1,2} X. Y. GAO ,¹ AND L. XIE ,¹

¹National Astronomical Observatories, Chinese Academy of Sciences, Jia-20 Datun Road, ChaoYang District, Beijing 100012, China

²School of Astronomy and Space Science, University of Chinese Academy of Sciences, Beijing 100049, China

³Key Laboratory of Radio Astronomy and Technology, Chinese Academy of Sciences, Beijing 100101, China

ABSTRACT

The turbulent ionized interstellar medium diffracts radio waves and makes them propagate in multiple paths. The pulse-broadening observed at low frequencies results from the scattering effect of interstellar clouds of ionized gas. During the Galactic Plane Pulsar Snapshot (GPPS) survey and other projects by using the Five-hundred-meter Aperture Spherical radio Telescope (FAST), we detect the pulse-broadening for 122 pulsars in the radio frequency band between 1.0 and 1.5 GHz, including 60 newly discovered pulsars in the GPPS survey and 62 previously known pulsars. We find that a more accurate dispersion measure can be obtained from aligning the front edge of the scattered subband pulses at the 1/4 or 1/2 peak level for most pulsars with one dominant component in the intrinsic profile, and the best DM values from aligning the intrinsic profile components from the model-fitting. From the pulse profiles at a few subbands we derive the pulse-broadening timescale and the scattering spectral index. These scattering parameters are measured for the first time for 93 pulsars. For 29 pulsars with previously detected scattering features, our measurements of the pulse-broadening timescale are consistent with results in the literature. We find that pulsars behind spiral arms show a stronger scattering effect due to greater density fluctuations in the arm regions. With a properly derived dispersion measure and careful calibration, we also present polarization profiles for 41 pulsars in three subbands of FAST observations.

Keywords: pulsars: general — ISM: scattering — Galaxy: general

1. INTRODUCTION

Ionized gas in the interstellar medium can cause two kinds of effects when radio pulses from pulsars pass through. One is the dispersion effect on the pulses, which causes a longer delay of pulses at lower frequencies. The more electrons accumulated along the path, the larger the pulse delay. The dispersion measure (DM) for pulses is thus defined as $DM = \int_{\text{psr}}^{\text{us}} n_e(l)dl$, in units of pc cm⁻³. Here $n_e(l)$ is the electron density at a distance l in units of cm⁻³, and dl is the unit length along the line of sight in pc. The distribution of electron density in the Milky Way can be described by the NE2001 model (Cordes & Lazio 2002) and YMW16 model (Yao et al. 2017). For most pulsars without distance measurements, their pulsar distances can be estimated from observed DM values by using the models. The second effect is the scattering caused by the irregular distribution of ionized gas clouds, which leads to multipath propagation of radio waves (Scheuer 1968) and is shown by the angular broadening of the point source, the intensity scintillation in the frequency and time domain, and the pulse broadening (see Rickett 1977, 1990, and references herein).

* E-mail: hjl@nao.cas.cn

The scattering effect broadens the intrinsic narrow pulses asymmetrically, so that the scattered profile can be expressed by the convolution of the intrinsic profile with a pulse broadening function (PBF) (Staelin 1970):

$$\text{PBF}(t) = \tau_s^{-1} \exp(-t/\tau_s) U(t) \quad (1)$$

where τ_s represents the pulse-broadening timescale, and $U(t)$ is the Heaviside step function (Bhat et al. 2004). This PBF assumes a thin screen in the middle between the pulsar and the observer (Cronyn 1970). The thin-screen model is generally used to describe the interstellar scattering (e.g. Cordes et al. 1985; Oswald et al. 2021). The pulse-broadening timescale τ_s depends on the observing frequency ν , and is typically described by a power-law relation (e.g. Bernadich et al. 2024):

$$\tau_s(\nu_{\text{GHz}}) = \tau_{1\text{GHz}} \cdot \nu_{\text{GHz}}^{-\alpha} \quad (2)$$

where α is the scattering spectral index.

Previously, Löhmer et al. (2001) and Li & Han (2003) used the unscattered profile at a high frequency as the intrinsic profile to measure or model the pulse-broadening at lower frequencies. Lewandowski et al. (2015b) allows the possible evolution of the profile components with frequency and then fits data for τ_s . Nice et al. (2013) simultaneously fit the intrinsic profile, pulse-broadening timescale at 1 GHz and DM by assuming $\alpha = 4$. Fonseca et al. (2024) tried to fit pulse

profiles in the 2-D frequency-time waterfall plot for fast radio bursts and radio pulsars. The pulse-broadening timescale τ_s at 1 GHz, $\tau_{1\text{GHz}}$ and the scattering spectral index α are two conventional characteristic parameters to describe the scattering effect. For the Kolmogorov turbulence, one should get $\alpha = 4.4$ (Rickett 1990). For the Gaussian turbulence, $\alpha = 4.0$ (e.g. Lee & Jokipii 1975a,b). The α derived from observations typically has a value around 4.0 with a deviation of about 0.6 (Oswald et al. 2021).

The pulse-broadening timescale τ_s is related to observed DMs of pulsars. It varies with $\text{DM}^{2.2}$ for the turbulent density distribution with a Kolmogorov spectrum, or $\text{DM}^{2.0}$ for the medium with a Gaussian spectrum (Rickett 1977). The DM dependence is not linear, and the observed τ_s – DM relation shows a steeper slope at high DM values than $\text{DM}^{2.2}$ (e.g. Sutton 1971; Bhattacharya et al. 1992; Ramachandran et al. 1997). Considering the frequency dependence and DM dependence together, one can get a joint empirical formula, e.g.

$$\log(\tau_s) = a + b(\log DM) + c(\log DM)^2 - \alpha \log \nu_{\text{GHz}} \quad (3)$$

by Bhat et al. (2004), where $a = -6.46$, $b = 0.154$, $c = 1.07$ and $\alpha = 3.86 \pm 0.16$, or

$$\tau_{1\text{GHz}} = 1.9 \times 10^{-7} \text{ ms} \times DM^{1.5} \times (1 + 3.55 \times 10^{-5} DM^3) \quad (4)$$

by Cordes et al. (2022). The data are scattered from this relation by 0.76 dex. The slope against DM becomes slightly steeper at higher DM due to the large density fluctuations in the inner Galaxy (Xu & Zhang 2017; Dexter et al. 2017; Cordes et al. 1985, 2016). Observed values of τ exhibit a spread of about two orders of magnitude around the empirical curves (Cordes et al. 2022). This is because of various fluctuations. On the one hand, there are large-scale electron density fluctuations distribution in the Galactic disk, halo and spiral arms. On the other hand, there are the small-scale density fluctuations caused by supernova shocks, stellar winds, HII regions (Taylor & Cordes 1993; Cordes & Lazio 1997, 2001, 2002, 2003; Ocker et al. 2021; He et al. 2025).

The scattering effect not only broadens the pulse profile but also redistributes the polarized emission into profile tails. The polarization profiles can be explained as the original profiles convolved with the PBF (Komesaroff et al. 1972). As a result, the polarization position angle (PA) curve tends to be flattened for the exponential tail of the profile (Li & Han 2003). This has been further verified by more observations (e.g. Karastergiou 2009), including the data in this paper.

Currently, the Five-hundred-meter Aperture Spherical radio Telescope (FAST) (Nan 2006; Nan et al. 2011) is the most sensitive telescope in the world. Since 2019 it has been working for many pulsar projects, including the Galactic Plane Pulsar Snapshot (GPPS) survey (Han et al. 2021). Up to now, more than 750 new pulsars have been discovered by this survey (Han et al. 2021, 2024). FAST has also been used for many related pulsar studies, such as the polarization measurements of 682 pulsars (Wang et al. 2023), the HI absorption measurements of a pulsar (Jing et al. 2023), de-

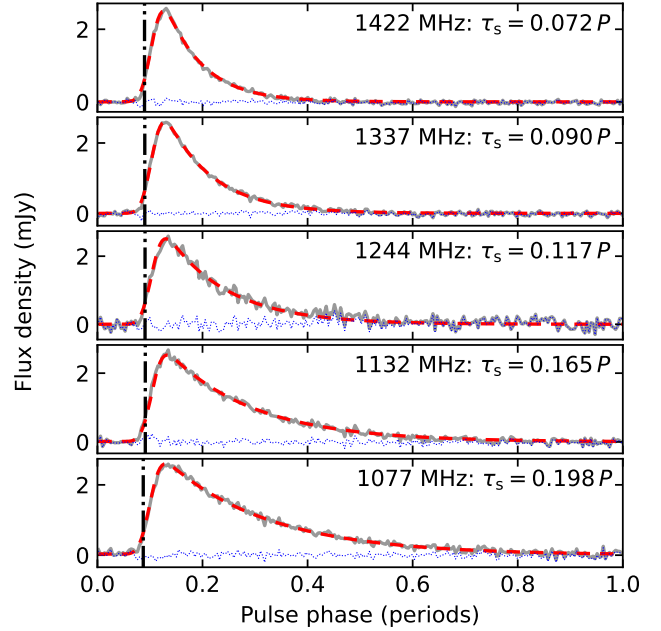


Figure 1: An example for fitting scattered features for sub-band profiles of FAST observations. The observed profiles (solid grey line) for PSR J2052+4421g are presented for 4 subbands. The fitted (dashed) profiles are obtained by a Gaussian function convolved with the standard PBF. The central frequencies and pulse-broadening timescales expressed as a fraction of the pulsar period, are marked in each sub-panel for a sub-band profile.

tection of dwarf pulses (Chen et al. 2023b; Yan et al. 2024), observations for mode-changing of pulsars (Yan et al. 2023) and pulsar timing (Su et al. 2023).

This paper presents the database of scattering profiles for 122 pulsars observed by the FAST during the FAST GPPS survey (Han et al. 2021, 2024) and other projects by the co-authors (e.g. Xu et al. 2022). Among them, 60 pulsars were discovered by the GPPS survey. Section 2 describes the FAST observations and data processing, including a method to get better DM values from the scattered signals than those from conventional routines. Section 3 presents the results and relevant discussion. Conclusions are given in Section 4.

2. FAST OBSERVATIONS AND DATA PROCESSING

All observations have been carried out by using the FAST L-band 19-beam receiver (Jiang et al. 2020), which works in the radio band of 1.0 – 1.5 GHz. The digital bands can record the 4 (XX , YY , $\text{Re}[X^*Y]$ and $\text{Im}[X^*Y]$) or 2 (XX , YY) polarization channel data for all 2048 frequency channels covering the band with a sampling time of 49.152 μs . Polarimetric calibration is achieved using the amplitude-modulated noise signals with a period of 2.01326592 s and a duty cycle of 50% (Wang et al. 2023).

Folding pulsar data and polarimetric calibration were processed in the following steps. Data from frequency channels at the lower edge covering a band of 45 MHz and at the

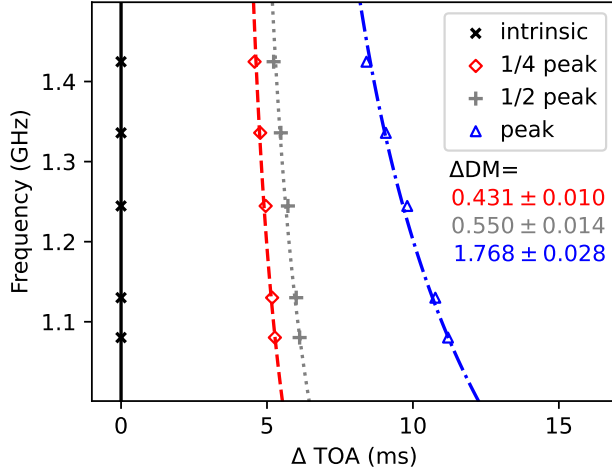


Figure 2: TOA delays for subband profiles for PSR J2052+4421g measured by using the DM values from aligning the peak, the lead edge at the half peak level (1/2) and at the quarter peak level (1/4), compared to TOA from the exactly de-convolved intrinsic profile component alignment without scattering delay. There is a small DM offset caused by different alignments, depending on the pulsar period, as indicated inside a plot.

higher edge covering a band of 30 MHz have been discarded because of the low gains (Jiang et al. 2020). The data are first folded into a pulse stack by using *DSPSR* (van Straten & Bailes 2011), based on the pulsar ephemeris from the Pulsar Catalogue (Manchester et al. 2005). For pulsars without timing solutions, we use *PDMP* from *PSRCHIVE*¹ (Hotan et al. 2004) to get the best pulsar period. Radio frequency interference (RFI) in some channels is mitigated manually by using *PAZ* (van Straten et al. 2012) or automatically by using the new tool *2σCRF* (Chen et al. 2023a).

When a pulsar is strongly scattered, the pulse is much more broadened at lower frequencies. Ideally, profiles with high signal-to-noise ratios from very fine frequency channels over a wide frequency range are needed to fit the scattering model. In practice, a compromise has to be made on the bandwidth and signal-to-noise ratio. In practice, we measure the scattering parameters using 3 to 5 subband profiles of the FAST pulsar observations, depending on signal strength and RFI situation, and then use the 32 subband data to verify the results.

2.1. Preliminary determination of DM from scattering profiles

Obtaining unbiased DM measurements can be rather difficult for highly scattered pulsars. An incorrect DM value can lead to the misalignment of scattering profiles. The conventional method for measuring pulsar DM is to align the pulse peaks of all subband profiles. For broadened pulses

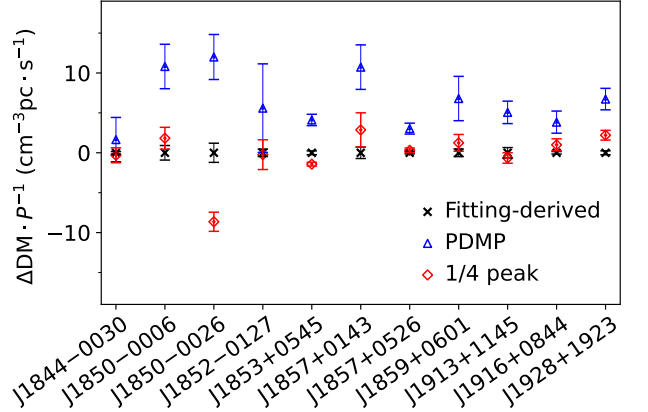


Figure 3: Comparison of DM estimates derived by using three alignments: DM values in the 2-D fitting (Oswald et al. 2021), the DM value directly measured by the *PDMP* tool (based on the peak alignment), and the DM value from the front-edge alignment at the 1/4 peak level.

with shifted peaks at lower frequencies (Oswald et al. 2021), such a method causes a large systematic deviation of a real DM value.

To minimize the DM bias, some new methods have been proposed, either through fitting profiles based on specific assumptions (Geyer et al. 2017; Andersen et al. 2023) or by using data-driven methods that avoid excessive assumptions about PBFs and intrinsic profiles (e.g. Hessels et al. 2019). For pulsars with a single dominant component scattered with the pulse broadening function of an exponential function given by the thin screen discussed above, we can get a DM by straight-forwardly aligning the leading edge at a half (1/2) or a quarter (1/4) level of the peak, as demonstrated in Fig. 1. This method was first presented by Ables et al. (1970). We evaluate the possible DM offsets by different alignments of the scattered profile of PSR J2046+4253g, a newly-discovered pulsar by the FAST GPPS survey. To remove white noise from subband profiles, we simultaneously fit the pulse-broadening timescale at 1 GHz $\tau_{1\text{GHz}}$ and the scattering spectral index α , assuming the same intrinsic profile across the observing band, similar to Nice et al. (2013).

The observed and fitted subband profiles are aligned well in Figure 1. Using these scattering parameters, we generate a noise-free waterfall plot that can reveal the frequency-dependent times of arrival (TOAs) for the half and quarter-level alignment of the front edges and the peak positions for all sub-band profiles, with an example shown in Figure 2, which in fact cause different systematic DM deviation. Taking the DM values from the careful 2-D fitting method (Oswald et al. 2021) as the reference, we compare the DM values obtained from the normal *PDMP* in the *PSRCHIVE* package and the 1/4 peak level alignment, as shown in Fig. 3, and find that the DM values obtained by the 1/4 peak alignment are much better than those obtained by the *PDMP* and the offset is almost ignorable if the intrinsic profiles and PBFs are properly assumed.

¹ <http://psrchive.sourceforge.net>

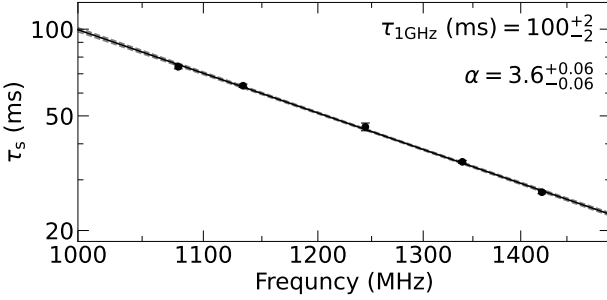


Figure 4: Fitting the pulse-broadening timescale τ_s to get the scattering spectral index α . The pulse-broadening timescales are obtained from Fig. 1 using the technique described in Section 2.2.1. From such a power-law fitting, one can get the frequency dependence of τ_s and α (with the $\pm 1\sigma$ uncertainties).

2.2. Jointly fitting subband profiles for DM and scattering parameters

The DM of a scattered pulsar preliminarily obtained by aligning the leading edge of subband profiles at the half or quarter peak power level can be used for the further joint fitting of DM-corrected subband profiles for the pulse-broadening timescale and new DM iteratively.

There are four methods in literature to get the pulse-broadening timescale from the scattering profiles: (1) directly fitting the observed profiles using the convolution of the best-trial intrinsic profile and the PBF (e.g. Cordes et al. 1985; Kuzmin & Losovsky 2007); (2) the deconvolution of the scattering profiles by using the “CLEAN” method (e.g. Bhat et al. 2003; Young & Lam 2024); (3) the deconvolution of the profiles in the Fourier domain (Kuz’min & Izvekova 1993); (4) the coherent cyclic spectral analysis to resolve the frequency-dependent time delay due to multipath propagation from base-band data (e.g. Demorest 2011). The last method works on the base-band data, which is not applicable here. The deconvolution method and the clean method can work well on subband profiles with high signal-to-noise ratios (S/Ns), while our subband profiles do not always have high S/Ns. Because our subband profiles have a wide range of signal-to-noise ratios, we use the direct fitting method and acknowledge the possible parameter bias related to the assumed intrinsic profile. Fortunately, most pulsars have one dominant profile component or two or three components that can be easily figured out from the highest-frequency subband profile. The thin screen model can describe the scattering medium for most pulsars.

We fit subband profiles for the typical pulse-broadening timescale at 1 GHz, the scattering spectral index α and the model DM iteratively. The details are outlined below.

2.2.1. Fitting the subband profiles independently

The pulse-broadening timescale τ_s in each subband can be directly obtained from the fitting on each subband profile (Geyer et al. 2017; Oswald et al. 2021). Then, one could get

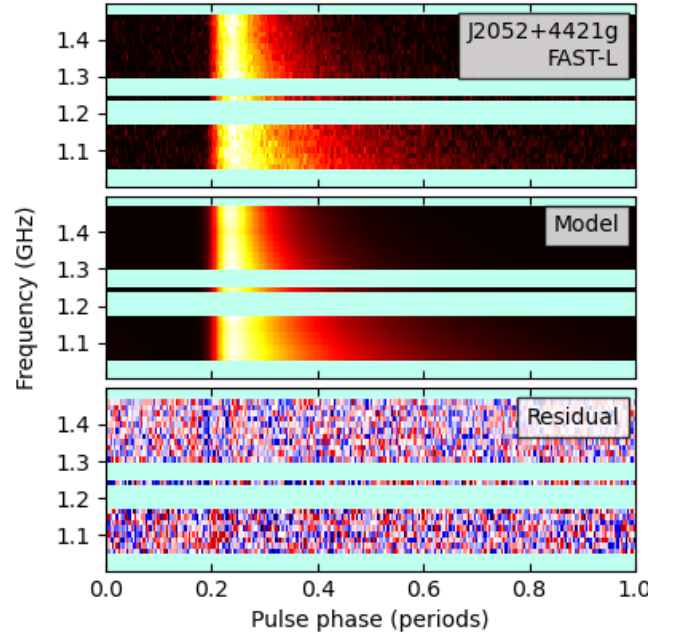


Figure 5: Comparison with the observed 32-subband data by the FAST (top panel) with the modeled profiles (middle panel) produced by the fitted scattering parameters. The scattering parameters should have been reasonably obtained if the residual image (bottom panel) is random and has no obvious structure. Here is only an example for PSR J2025+4421g, and some channels with RFI have been discarded. Comparisons for all pulsars are presented in Fig. A1.

the scattering spectral index α from these fitted timescales for these subbands.

The observed subband profiles are modeled as the convolution of the intrinsic profile, the PBF and also the instrumental smearing function. The intrinsic profile is assumed to be a sum of multiple Gaussian components, $\Sigma G(t)$ (Kramer 1994), where t is the pulse phase. Each Gaussian component has three free parameters: amplitude A , center phase μ , and the characteristic width σ (Oswald et al. 2021). The number of Gaussian components is initially obtained from the subband profile at the highest frequency suffering the least scattering effect, and we limit the number to no more than 3 components to avoid over-fitting (Bansal et al. 2019). The PBF is modeled as an exponential decay as Equation 1 representing the interstellar medium scattering effect (Löhmer et al. 2001, 2004). Instrumental smearing effects (Voûte et al. 2002) are described by the rectangular functions representing intra-channel dispersion $D(t)$ and sampling time $S(t)$. Thus, the scattered profile of each subband is then modeled by

$$I(t) = S(t) \otimes D(t) \otimes \text{PBF}(t) \otimes \Sigma G(t), \quad (5)$$

here \otimes denotes the convolution. A flat baseline is included for cases where the scattering tail is sufficiently long to spread energy across the entire phase of pulsar rotation (Geyer & Karastergiou 2016). The subband profiles from different subbands are fitted independently using the differ-

Table 1: Fitted scattering parameters for 121 pulsars derived from FAST observations

PSR Name	<i>l</i> (°) (1)	<i>b</i> (°) (2)	<i>P</i> (ms) (4)	FAST Obs. Date yyyy-mm-dd (5)	<i>T</i> _{obs} (s) (6)	DM _{1/4} (cm ⁻³ pc) (7)	DM (cm ⁻³ pc) (8)	$\tau_{1\text{GHz}}$ (ms) (9)	α (10)
J1833–0204g	29.022	3.050	4.43	2021-10-18	900	312.1(1)	312.08(4)	0.8(1)	3.2(7)
J1841–0157	30.099	1.216	663.38	2021-09-01	900	473.4(3)	473.5(4)	14.44(6)	3.50(2)
J1842–0153	30.283	1.022	1054.32	2021-09-03	900	424.3(6)	423.8(7)	31.4(2)	3.38(3)
J1842–0258g	29.202	0.738	596.30	2023-10-26	900	355.7(9)	355.7(7)	20.7(5)	3.7(1)
J1842–0309	29.077	0.584	404.95	2023-10-26	900	943.6(17)	948(1)	82(3)	3.8(2)
J1843–0050	31.295	1.360	782.66	2021-10-09	900	511.6(7)	511.6(4)	15.5(3)	3.61(6)
J1843–0137	30.543	1.087	669.88	2021-09-23	900	483.3(6)	483.4(8)	25.5(3)	3.53(4)
J1843–0157g	30.294	0.847	508.90	2021-08-22; 2021-09-03	1200	751(2)	751(2)	110(5)	3.4(2)
J1844–0030	31.710	1.271	641.15	2020-04-21	900	603.1(7)	603.0(7)	11.0(2)	3.19(5)
J1844–0136g	30.685	0.843	417.27	2024-04-21	900	901(4)	903(2)	73(7)	4.2(3)
J1844–0142g	30.587	0.847	348.74	2021-09-23; 2021-10-18; 2021-11-11	2100	794.5(15)	794.4(9)	28(2)	4.9(2)
J1844–0202g	30.269	0.720	761.45	2023-02-18	900	628(6)	628(6)	64(7)	4.5(5)
J1844–0240	29.804	0.254	581.55	2022-11-20	300	315(5)	315(3)	64(5)	3.3(3)
J1844–0244	29.727	0.235	507.72	2022-11-20	300	422.0(6)	422.0(6)	20.3(3)	3.48(5)
J1844–0256	29.574	0.119	273.00	2022-11-20	300	819(2)	820.0(7)	98(5)	3.8(2)
J1844–0302	29.395	0.243	1198.63	2022-11-20	300	542(2)	542(2)	29(2)	4.4(3)
J1844–0310	29.343	0.036	525.02	2021-02-21	600	827(2)	827.8(7)	73(4) [†]	4.1(2) [†]
J1845–0103g	31.272	0.847	99.07	2021-10-22; 2021-11-11	1200	750.1(6)	750.6(2)	34(1)	4.46(10)
J1845–0142g	30.734	0.593	126.19	2022-01-20; 2022-01-30	1200	564(4)	563.1(6)	52(12)	3.1(7)
J1845–0144g	30.709	0.466	593.94	2021-12-25; 2022-01-13; 2022-01-30	2100	937.7(14)	937.7(14)	216(5)	4.14(8)
J1845–0229Ag	30.024	0.212	657.72	2022-11-27	900	832(5)	842(4)	238(22)	4.6(3)
J1845–0229Bg	30.098	0.085	463.05	2023-05-30	900	846(31)	876(7)	234(65)	5.1(9)
J1845–0243g	29.828	0.066	345.26	2023-05-26	900	747(4)	750(2)	191(24)	5.1(5)
J1845–0254g	29.677	-0.012	492.65	2023-07-06	900	735(35)	769(7)	516(74)	4.7(5)
J1845–0316	29.391	-0.255	207.64	2025-04-11	300	495.1(4)	495.1(3)	21(1)	5.1(2)
J1846–0211g	30.391	0.166	788.17	2022-09-02	900	838(3)	838(4)	114(8)	5.1(3)
J1848–0055	31.797	0.171	274.58	2021-10-24	300	1155(2)	1157.8(14)	119(9)	4.0(3)
J1849–0013	32.501	0.338	491.75	2020-08-15	900	343.6(9)	345.1(6)	71(3)	4.2(2)
J1849–0040	32.075	0.198	672.54	2021-01-30; 2021-11-11	1200	1265(4)	1265(4)	278(13)	4.9(2)
J1849–0200g	31.000	0.600	326.76	2022-06-11	900	883(4)	887(3)	160(33)	2.3(6)
J1850–0002	32.823	0.356	893.35	2022-11-06	3400	537(4)	537(2)	42(1)	3.4(1)
J1850–0006	32.764	0.093	2191.30	2020-02-23; 2020-08-21	1200	632(2)	629(3)	229(3)	3.70(4)
J1850–0020	33.081	0.453	1574.70	2021-01-30; 2020-04-01; 2020-04-02; 2020-08-01; 2020-08-19	3900	598(2)	598(2)	34(1)	3.6(2)
J1850–0026	32.407	0.066	166.64	2020-04-02; 2020-08-01; 2020-08-19	2700	947.0(2)	947.5(2)	35.6(4) [†]	4.19(4) [†]
J1850–0031	32.369	0.041	734.15	2020-04-02; 2020-08-01; 2020-08-19	2700	895.0(16)	895(2)	105(2)	4.68(5)
J1850–0050g	32.103	-0.170	221.54	2021-09-03; 2021-10-09	1800	1060(4)	1064(2)	157(9)	4.3(2)
J1850+0242	35.265	1.403	4.48	2020-12-22	300	539.7(8)	539.7(2)	5.9(7)	4.8(4)
J1851–0029	32.542	0.335	518.68	2021-02-11; 2021-03-06	600	519.5(3)	519.5(3)	13.3(2)	3.42(5)
J1851–0108g	31.883	-0.466	87.09	2021-09-23; 2021-10-05	1200	669.6(6)	669.6(4)	25(2)	4.6(3)
J1851–0241	30.515	1.186	435.19	2022-11-22	300	511(3)	511(2)	105(9)	4.1(3)
J1851+0233	35.181	1.232	344.02	2020-05-28	300	606(8)	610(3)	84(18)	4.1(7)
J1852–0127	31.706	-0.802	429.01	2021-09-01	300	427.7(7)	427.9(9)	66.2(8)	3.89(4)
J1852+0013	33.282	0.174	957.75	2020-04-17; 2020-08-11; 2020-08-17; 2020-09-20	3600	542.7(3)	542.7(3)	21.3(2)	3.63(4)
J1852+0018	33.326	-0.085	318.77	2019-08-25; 2020-04-17; 2020-09-15	2100	452.9(7)	452.9(8)	20(2)	3.7(3)
J1852+0031	33.523	0.017	2180.47	2020-08-16; 2021-11-14	1800	752.0(15)	745.6(13)	803(2)	3.720(8)
J1852+0056g	33.864	0.254	1177.91	2020-04-04; 2020-08-19; 2020-08-20; 2020-09-11; 2020-11-06; 2021-02-07; 2022-02-07	6300	893.4(12)	893.6(15)	118(3)	4.82(8)
J1852+0309g	35.821	1.271	5.58	2021-03-06	900	358.0(4)	358.18(6)	3.6(6)	4.3(7)
J1853–0049g	32.389	-0.731	16.78	2022-05-09	900	405.4(4)	405.6(2)	5.4(12)	3.8(8)
J1853–0054g	32.421	-0.974	308.35	2021-12-21; 2022-01-13	1200	441.6(6)	441.6(8)	17(1)	4.0(2)
J1853+0237g	35.552	0.635	427.36	2020-04-19; 2021-03-20	1200	715(7)	718(2)	78(9)	4.5(5)
J1853+0505	37.650	1.956	905.06	2021-04-22	300	263.0(5)	260.4(6)	209(1)	3.60(2)

... to be continued.

Table 1: – *continued*

PSR Name	<i>l</i> (°) (1)	<i>b</i> (°) (2)	<i>P</i> (ms) (3)	FAST Obs. Date yyyy-mm-dd (5)	<i>T</i> _{obs} (s) (6)	DM _{1/4} (cm ⁻³ pc) (7)	DM (cm ⁻³ pc) (8)	τ_{GHz} (ms) (9)	α (10)
J1853+0545	38.353	2.064	126.41	2020-08-01	300	197.72(3)	197.73(4)	20.9(1)	3.89(2)
J1854+0131g	34.647	0.000	2043.73	2020-02-17; 2020-08-17; 2020-09-10; 2020-10-05	3000	451(8)	450(8)	607(27)	3.0(2)
J1854-00	33.849	-0.394	716.87	2020-04-20	300	492(2)	491.7(17)	18.0(5)	2.8(1)
J1855-0221g	31.345	-2.076	2.77	2023-03-05	900	223.25(7)	223.32(4)	0.8(2)	4.4(7)
J1855+0205	35.281	0.007	246.83	2019-09-13	300	866.1(8)	866.1(6)	17.8(3)	3.4(2)
J1855+0422	37.314	1.052	1678.11	2020-12-04	300	453.9(9)	449(1)	50.5(9)	4.60(8)
J1855+0455g	37.753	1.398	101.01	2020-08-13	900	372(2)	372.0(5)	21(2)	3.8(4)
J1855+0511g	37.985	1.534	1421.47	2024-02-17	900	285(2)	284.7(18)	160(4)	3.72(10)
J1855+0527	38.227	1.642	1393.47	2020-04-19	300	353(3)	353(3)	99(4)	3.9(2)
J1856+0245	36.007	0.057	80.91	2020-11-04	600	621(2)	619.1(6)	29(4)	4.9(6)
J1857+0143	35.168	-0.571	139.79	2019-09-17	300	248.5(4)	248.3(2)	41.5(9)	3.39(8)
J1857+0210	35.586	-0.393	630.97	2021-11-07	300	778.8(6)	778.9(8)	32.0(9)	4.6(2)
J1857+0214	35.577	-0.241	333.92	2020-02-12; 2020-08-22	1800	972(12)	982(7)	196(43)	2.7(7)
J1857+0300	36.274	0.072	772.68	2020-05-20	300	690(2)	690(2)	18(2)	4.9(4)
J1857+0526	38.438	1.187	349.96	2020-05-14; 2021-08-26	1800	464.85(10)	465.1(1)	24.0(3)	3.82(4)
J1858+0215	35.725	-0.493	745.76	2020-04-19	300	697(1)	697(1)	42(2)	3.1(2)
J1858+0244g	36.122	-0.212	2.61	2021-12-10	900	282.45(4)	282.57(3)	1.6(2)	5.3(5)
J1859+0430	37.819	0.343	336.32	2020-04-02	900	780(4)	780(2)	24(3)	4.0(6)
J1859+0601	39.245	0.903	1044.24	2020-03-04; 2020-08-21	1500	273.5(11)	273.8(13)	68(3)	2.9(2)
J1900+0438	38.067	0.169	312.29	2020-04-04; 2020-08-15	1800	622(4)	623(3)	193(17)	4.8(3)
J1901+0459	38.490	0.087	877.07	2020-12-19	600	1100(6)	1100(5)	121(12)	4.8(4)
J1902-0107g	33.211	-2.996	6.12	2022-07-21	900	290.2(2)	290.02(8)	2.6(3)	3.4(5)
J1903+0327	37.336	-1.014	2.15	2020-05-23	900	297.526(9)	297.533(4)	0.45(3)	4.3(5)
J1905+0600	39.838	-0.277	441.25	2020-02-19	300	727.1(5)	727.1(5)	19.7(2)	3.80(4)
J1907+0534	39.717	-0.988	1138.32	2020-05-14	300	522.7(7)	522.7(7)	20.5(4)	3.41(9)
J1908+0833	42.469	0.171	512.15	2020-10-26	300	698(2)	698(2)	35(2)	4.6(3)
J1908+0839	42.560	0.229	185.41	2020-10-26	600	513.3(2)	513.3(3)	8.9(1)	2.75(5)
J1908+0909	42.972	0.494	336.55	2019-12-26	300	465.3(2)	465.3(2)	7.4(2)	2.36(6)
J1910+0534	40.056	-1.668	452.85	2021-06-21	300	478.2(5)	478.2(6)	14.4(2)	2.97(5)
J1910+1026	44.438	0.504	531.59	2020-09-01; 2020-11-23	1200	714.0(12)	713.9(13)	23(2)	3.3(2)
J1911+0101A	36.111	-3.918	3.62	2021-11-19	750	202.54(2)	202.56(1)	0.42(1)	3.38(10)
J1911+0925	43.675	-0.220	323.87	2020-08-06	900	481(3)	481(2)	48(7)	4.0(5)
J1913+1000	44.285	-0.194	837.15	2020-12-06; 2021-01-13	1200	422(1)	419.5(5)	18.6(3)	4.0(2)
J1913+1102	45.250	0.194	27.27	2021-11-18	600	339.0(8)	338.7(2)	12(2)	3.6(6)
J1913+11025	45.286	0.127	923.90	2020-12-04; 2020-12-28; 2021-11-18	2100	620(2)	620(2)	68(6)	2.6(3)
J1913+1145	45.920	0.476	306.05	2020-05-23	300	641.9(2)	641.9(2)	15.9(2)	4.19(5)
J1914+1054g	45.213	-0.000	138.87	2020-12-28	900	417.6(6)	417.6(7)	12(2)	4.0(6)
J1916+0844	43.538	-1.493	440.02	2020-12-15	300	338.6(2)	338.5(3)	12.27(8)	3.34(3)
J1918+1340g	48.197	0.254	232.98	2020-08-07	900	572.6(4)	572.6(3)	26.3(7)	4.6(2)
J1919+1314	47.895	-0.088	571.45	2021-10-12	300	612.4(6)	612.4(7)	17.2(6)	2.89(10)
J1919+1341	48.251	0.168	11.66	2020-03-03; 2020-08-07; 2021-05-13; 2021-06-29; 2021-06-29; 2021-07-15; 2021-11-14; 2021-12-26; 2022-01-05; 2022-05-29; 2022-06-25; 2022-11-05; 2023-01-24; 2023-02-09; 2023-03-08; 2023-08-08; 2023-08-09; 2023-08-10; 2023-08-15; 2023-08-19; 2023-08-23; 2023-08-26; 2023-08-28; 2023-10-14; 2023-11-10; 2024-01-19; 2024-01-30	27000	394(1)	394.0(3)	2.1(1)	4.7(3)
J1920+1110	46.152	-1.199	509.92	2020-05-09	300	186.7(5)	186.7(6)	20.7(3)	3.58(5)
J1920+1340g	48.334	-0.005	1525.92	2023-10-14	900	1053(24)	1053(7)	352(38)	2.0(5)
J1921+1216g	47.214	-0.866	3.00	2023-11-26	900	256.09(2)	256.12(1)	0.97(7)	3.03(5)
J1921+1259g	47.873	-0.583	573.16	2024-02-17	900	357(3)	356.6(16)	38(2)	4.2(3)
J1921+1340g	48.515	-0.297	4603.04	2023-02-14	4590	723(5)	723(5)	160(5)	3.69(10)
J1921+1505g	49.738	0.381	611.90	2020-08-12	900	513(2)	510.6(16)	25(3)	4.3(5)

... to be continued.

Table 1: – *continued*

PSR Name	l (°)	b (°)	P (ms)	FAST Obs. Date yyyy-mm-dd	T_{obs} (s)	$\text{DM}_{1/4}$ (cm^{-3}pc)	DM (cm^{-3}pc)	$\tau_{1\text{GHz}}$ (ms)	α
(1)	(2)	(3)	(4)	(5)	(6)	(7)	(8)	(9)	(10)
J1922+1512g	49.933	0.212	2357.21	2022-05-12	900	395(2)	395(3)	78(2)	3.16(7)
J1924+1713	51.988	0.720	758.43	2020-08-08	900	539.0(13)	539(2)	39(2)	3.7(2)
J1928+1923	54.281	1.016	817.40	2020-08-03	300	478.2(5)	476.4(5)	48.2(5)	3.78(4)
J1946+2433g	60.915	-0.254	8.57	2022-02-02	900	275.2(7)	275.20(9)	4.6(12)	4.8(10)
J1946+2757g	63.847	1.487	742.99	2021-07-07; 2021-07-22	1800	458(3)	450(2)	125(5)	3.1(2)
J1950+2414	61.111	-1.186	4.30	2020-05-13	300	142.04(2)	142.08(2)	0.88(4)	3.2(3)
J1959+3141g	68.424	1.083	514.53	2023-08-25	900	340.6(10)	340.7(2)	15.3(6)	3.8(2)
J2004+3429	71.425	1.571	240.99	2020-04-19	600	354.1(2)	354.1(3)	11.5(1)	4.16(5)
J2005+3411g	71.261	1.229	651.04	2020-08-08; 2021-11-14	1800	483.0(4)	483.0(4)	42.6(10)	3.83(6)
J2015+3404g	72.255	-0.466	4.28	2023-01-06	900	207.98(4)	208.05(4)	1.6(2)	2.8(3)
J2019+3718g	75.379	0.690	505.23	2023-10-17	900	461.6(5)	461.6(7)	24.0(3)	4.28(5)
J2021+3651	75.222	0.111	103.77	2020-03-03; 2020-04-23	900	369.1(5)	369.2(5)	14.5(6)	2.9(2)
J2021+4024g	78.176	2.114	370.56	2020-08-12; 2020-10-13	1800	678.8(10)	678.8(5)	82.1(14)	3.3(3)
J2022+3845g	76.911	1.017	1008.87	2020-08-08; 2020-10-13	1800	483(2)	483(3)	258(8)	4.3(2)
J2030+3818g	77.449	-0.508	133.72	2021-03-17; 2021-08-11	1800	597.8(7)	596.8(3)	7.8(9)	2.0(5)
J2030+3944g	78.599	0.297	306.19	2020-08-10	900	934.7(10)	934.8(8)	114(4)	3.4(2)
J2032+4055g	79.838	0.646	48.74	2023-10-15	900	372.4(7)	373.7(5)	38(4)	3.1(4)
J2041+3934g	79.745	-1.470	379.97	2024-11-18	900	408(1)	408.2(13)	234(12)	4.8(2)
J2041+46	84.766	2.334	1160.00	2022-05-01	300	306(1)	306.2(16)	28.4(5)	3.50(2)
J2045+4431g	84.126	0.975	141.82	2024-11-18	900	428(5)	428.5(15)	16.6(9)	3.1(2)
J2046+4236g	82.756	-0.381	523.84	2023-10-15	900	466(10)	466(4)	273(62)	3.7(6)
J2046+4253g	83.016	-0.259	331.15	2022-09-07	900	622.1(8)	622.2(9)	127(4)	3.87(9)
J2052+4421g	84.836	-0.169	375.34	2020-06-07; 2020-08-12; 2021-11-14	2700	543.8(7)	543.8(9)	95(1)	3.46(4)
J2057+4557g	86.597	0.152	225.38	2023-11-23	300	457.0(16)	456.9(3)	48(1)	3.8(1)

NOTE— Columns (1) pulsar name, (2) Galactic longitude, (3) Galactic latitude, (4) spin period, (5) FAST observation dates. For some pulsars data from a few dates are added together to get the scattering parameters; (6) the total length of observations in seconds; (7) dispersion measure from the alignment of the front edge at the 1/4 peak level, (8) dispersion measure from the joint fitting, (9) typical pulse-broadening timescale at 1 GHz $\tau_{1\text{GHz}}$, (10) scattering spectral index α . † The scattering parameters of two pulsars are obtained from the model fitting of subband profiles, allowing the frequency evolution of profile components.

ent intrinsic profiles, as done by [Lewandowski et al. \(2013, 2015a,b\)](#).

In the practical fitting calculations, the least squares method *curve_fit* in the Python package *scipy* is used which provides an initial estimate of the fitting parameters for each subband profile. Subsequently, the Monte Carlo Markov Chain (MCMC) method *emcee* is implemented to refine the parameters and assess the fitting errors. The best-fit parameters and their errors are determined using the 50th, 16th, and 84th percentiles from the MCMC sampling (see [Oswald et al. 2021](#)). The convergence of the MCMC fitting has been visually inspected.

The pulse broadening timescales τ_s measured in this manner of 3 to 5 subbands are obtained, which are listed in Table A1 and then used for a further fitting with a power-law function by the MCMC method to get the scattering spectral index α and also the typical pulse-broadening timescale $\tau_{1\text{GHz}}$, as shown in Figure 4.

2.2.2. Joint fitting subband profiles

If one can restore the unscattered profiles at multiple frequencies, the DM of a scattered pulsar can be optimized (e.g. [Singha et al. 2024](#)). If the length of scattered profiles is larger than the pulsar periods, the baseline of the scattered profile (e.g. [Geyer et al. 2017](#)) is hard to measure. We do our best to

compensate for the baseline by a freely fitted porfile offset or simply skip the data from such subbands or channels. Here, we model the frequency dependence of scattered profiles by assuming the same intrinsic profile in the observing band between 1.0 and 1.5 GHz. Then, we perform the best fit for DM and scattering parameters to the subband profiles.

The intrinsic profile is first modeled from the subband profiles at the highest frequency, as done in the last sub-section. The modeled profile of each subband is the convolution of the PBF and the intrinsic profile. Next, when we fit subband profiles together, both ISM effects and intrinsic profiles are optimized simultaneously. The real DM is obtained from the alignment of the main peak of the modeled intrinsic profiles from all subbands.

The Monte Carlo Markov Chain (MCMC) method *emcee* is implemented to fit good subband profiles together. We get the model parameters and determine the uncertainties using the 50%, 16%, and 84% percentiles from the MCMC sampling (e.g. [Oswald et al. 2021](#)). The convergence of the MCMC has been visually inspected. A new DM is obtained by aligning the main peak of the modeled intrinsic profile components. The above steps are iterated until the DM value is consistent with the previous one in 1σ uncertainty. The final results for pulsar DM and scattering parameters are in the last three columns in Table 1.

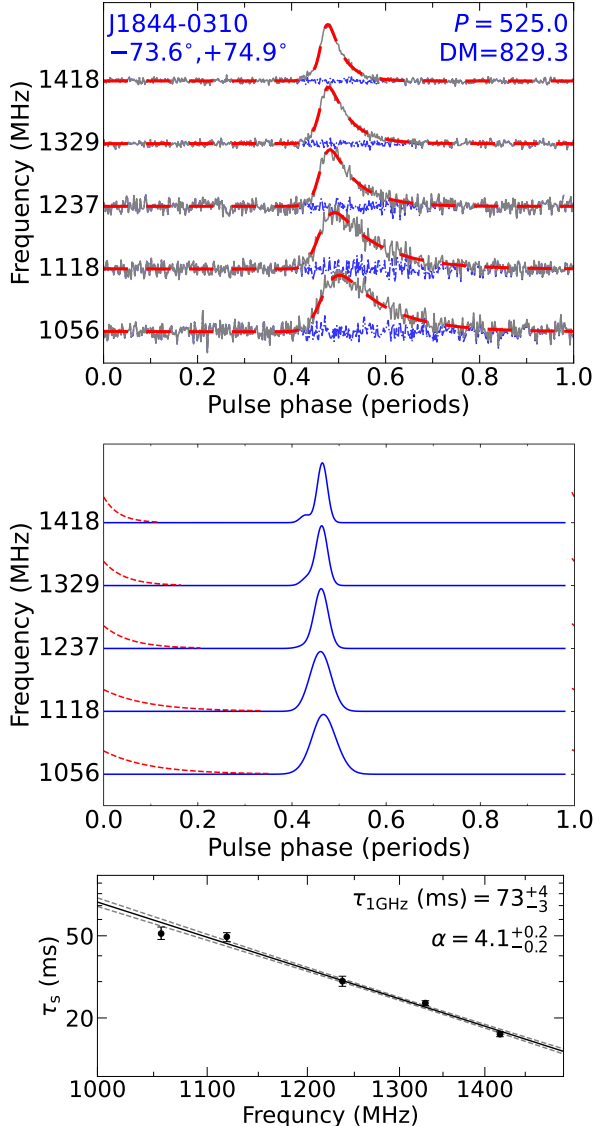


Figure 6: The subband profiles from the FAST observations for PSR J1844–0310 and the results for scattering parameter fittings. *Top panel*: profiles in solid lines and fittings in dashed lines for 5 subbands, together with residuals in short-dashed lines; *Middle panel*: the intrinsic subband profiles obtained from fittings in solid lines together with the PBFs in short-dashed lines; *Bottom panel*: the power-law fitting to the pulse-broadening timescales for the scattering spectral index α .

2.2.3. Validation of the fitting results by using the 2-D phase-frequency waterfall plot

The 2-D phase-frequency waterfall plot with 32 subbands in the FAST observation band of 1.0 – 1.5 GHz is used to evaluate the goodness of fitted scattering parameters. Based on the fitted parameters obtained above, we generate the model subband profiles and then scale them to match the observed subband profiles. For some channels or subbands, we

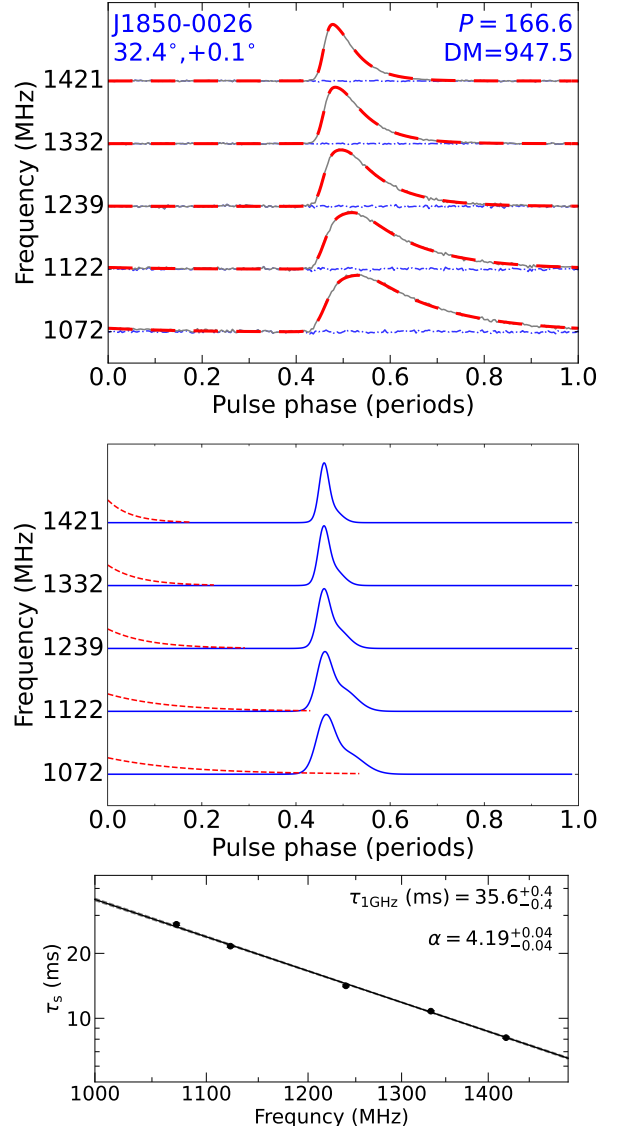


Figure 7: The same as Figure 6 but for PSR J1850–0026.

have to adjust the baselines of the profiles for several strongly scattered pulsars. After matching and subtracting, the residual waterfall plot should be random and have no structure as shown in Fig. 5 if the assumed intrinsic profiles with one, two or three components and the pulse-broadening functions are reasonable. For almost all cases, the joint fittings have produced excellent matching to the 2-D phase-frequency waterfall plots, as shown in Figure A1. There are only two exceptional cases in Figure A2, see details below.

2.2.4. Two exceptional cases

The two exceptional cases are PSR J1844–0310 and J1850–0026. Through simple joint fitting using the same intrinsic profiles, we got the scattering spectral indexes 5.7 ± 0.2 for PSR J1844–0310 and 5.76 ± 0.02 for PSR J1850–0026. Both of them show remarkable residuals in

Table 2: Comparison of pulse-broadening timescale and scattering spectral index from literature and obtained in this paper by FAST observations

PSR Name	Ref	ν_{Ref} (MHz)	τ_{Ref} (ms)	α_{Ref}	τ_{FAST} (ms)	α_{FAST}
(1)	(2)	(3)	(4)	(5)	(6)	(7)
J1842–0153	[1]	1000	32.7(3)	3.92(5)	31.4(2)	3.38(2)
J1844–0030	[1]	1000	12.3(3)	4.1(2)	11.0(2)	3.19(5)
J1844–0244	[1]	1000	20.0(4)	3.31(9)	20.3(3)	3.48(5)
J1850–0006	[1]	1000	260(7)	4.2(1)	229(3)	3.70(4)
J1850–0026	[1]	1000	46.5(6)	4.946(2)	35.6(4)	4.19(4)
J1852–0127	[1]	1000	57(3)	3.6(1)	66.2(8)	3.89(4)
J1852+0031	[3]	1175	495(25)	-	443.5(13)	3.720(8)
	[3]	1475	225(14)	-	190.3(9)	-
	[2]	2700	36(16)	2.8(10)	-	-
J1853+0505	[3]	1175	124(14)	-	117.0(7)	3.60(2)
	[3]	1475	54(3)	-	51.6(5)	-
J1853+0545	[1]	1000	20.0(3)	3.13(4)	20.9(1)	3.89(2)
	[3]	1175	13.6(20)	-	11.16(7)	-
	[3]	1475	7.1(9)	-	4.61(5)	-
	[3]	2380	1.5(2)	-	-	-
J1855+0205	[4]	1000	16.3(9)	-	17.3(5)	3.4(2)
J1855+0422	[3]	1175	27(3)	-	24.1(6)	4.60(8)
J1856+0245	[4]	1000	18.0(6)	-	29(4)	4.9(6)
J1857+0143	[1]	1000	50(2)	4.0(1)	41.5(9)	3.39(8)
	[5]	1170	24(5)	-	24.4(7)	-
	[5]	2600	0.05(1)	-	-	-
	[5]	4850	0.03(2)	-	-	-
J1857+0210	[3]	1175	13.4(36)	-	15.2(7)	4.6(2)
J1857+0526	[1]	1000	24.0(6)	3.78(7)	24.0(3)	3.82(4)
	[3]	1175	14.5(17)	-	13.0(2)	-
	[3]	1475	6.2(13)	-	5.44(10)	-
J1858+0215	[3]	1175	38(3)	-	25.5(15)	3.1(2)
	[3]	1475	18.4(47)	-	12.6(12)	-
J1859+0601	[1]	1000	125(26)	4.4(7)	68(3)	2.9(2)
J1903+0327	[6]	1400	0.126(1)	-	0.12(3)	4.3(5)
J1908+0839	[3]	1175	5.6(13)	-	4.4(2)	2.75(5)
	[3]	1475	2.6(6)	-	2.23(7)	-
J1908+0909	[3]	1175	4.9(9)	-	5.1(2)	2.36(6)
J1910+0534	[3]	1175	12.5(8)	-	8.9(2)	2.97(5)
J1911+0925	[7]	1000	38(8)	4.3(7)	48(7)	4.0(5)
J1913+11025	[7]	1000	51(4)	1.6(2)	71(8)	2.6(3)
J1913+1145	[1]	1000	15.2(7)	3.9(2)	15.9(2)	4.19(5)
	[3]	1175	9.2(10)	-	8.1(2)	-
	[3]	1475	4.3(5)	-	3.12(8)	-
J1916+0844	[1]	1000	12.8(1)	4.14(7)	12.27(8)	3.34(3)
	[3]	1175	7.7(10)	-	7.16(6)	-
	[3]	1475	3.6(9)	-	3.35(5)	-
J1919+1314	[4]	1000	18.7(9)	-	18.1(5)	2.89(10)
J1920+1110	[3]	1175	14.0(33)	-	11.6(2)	3.58(5)
	[3]	1475	6.3(21)	-	5.1(2)	-
J1924+1713	[7]	1000	39(18)	4.5(15)	39(2)	3.7(2)
J1928+1923	[1]	1000	48.6(5)	3.94(5)	48.2(5)	3.78(4)

NOTE— Columns (1) pulsar name, (2) reference for public scattering parameters, (3) central frequency of the pulse broadening timescale of the reference, (4) pulse-broadening timescale at the given frequency, (5) public scattering spectral index, (6) pulse-broadening timescale at the reference frequency interpolated by scattering parameters in this paper, (9) scattering spectral index measured by FAST. The references are marked as: [1] Oswald et al. (2021); [2] Löhmer et al. (2001); [3] Bhat et al. (2004); [4] Nice et al. (2013); [5] Lewandowski et al. (2013); [6] Champion et al. (2008); [7] Parent et al. (2022).

the 2-D phase-frequency waterfall plot, and the α value for PSR J1850–0026 is greater than that given by Oswald et al. (2021), as listed in Table 2. The extremely low and seemingly implausible error values observed for the two pulsars are likely the result of the fitting process converging to a local optimum. However, when we check the fitting to the profiles of individual subbands and the 2-D residual plots, we understand that there is a weak frequency-evolving component on the leading edge of PSR J1844–0310 and a weak component on the trailing edge of J1850–0026.

As shown in Figure 6, the weak leading component of PSR J1844–0310 becomes more prominent and is mixed with the main component at lower frequencies, making the main component broader at lower frequencies. By taking the frequency-evolved intrinsic profiles, we fit the observed subband profiles using the method in Section 2.2.1, we get the scattering parameters of $\tau_{1\text{GHz}} = 73 \pm 4$ ms and $\alpha = 4.2 \pm 0.2$.

The extra component on the trailing side of PSR J1850–0026 also has frequency evolution and causes more broadening of the observed profiles at the lower frequencies, not only the scattering tails, as shown in Figure 7. As done above, by taking the frequency-evolved intrinsic profiles, we fit the observed subband profiles using the method in Section 2.2.1, we get the broadening timescales for all subband profiles, and then fit the scattering parameters. Finally, we obtain $\tau_{1\text{GHz}} = 35.6 \pm 0.4$ ms and $\alpha = 4.19 \pm 0.04$.

We, therefore, understand that in some cases, only when the reasonable frequency evolution of profile components is considered in the model-fitting, can the scattering parameters be properly estimated.

3. RESULTS AND DISCUSSION

In total, we have measured the scattering parameters for 122 pulsars using data from GPPS and other FAST projects, as indicated by the lengthening tails at lower frequencies in Figure 1 and Figure 5. Plots for all 122 pulsars are presented in Figure A1. The fitted scattering parameters for all 122 pulsars are listed in Table 1, including two DM values respectively obtained by the front-edge alignment and joint fitting, $\tau_{1\text{GHz}}$, and α . It can be observed that DM values derived from the two approaches are consistent within the 3σ error.

3.1. Pulsar scattering parameters in literature and comparison with FAST measurements

To investigate the DM and direction dependence of scattering effects and to compare FAST-measured scattering parameters with the literature values, we have to collect all measurements of scattering parameters previously published. We noticed that He & Shi (2024) collected scattering times for 473 pulsars from 54 papers. In our full collection, 497 pulsars have the pulse-broadening timescale measured in the reference. We only use measurements of τ_s with a relative uncertainty better than 10 percent. Most of them are the reliable measurements from wide-band observations (Oswald et al. 2021) with prominent scattering features in profiles.

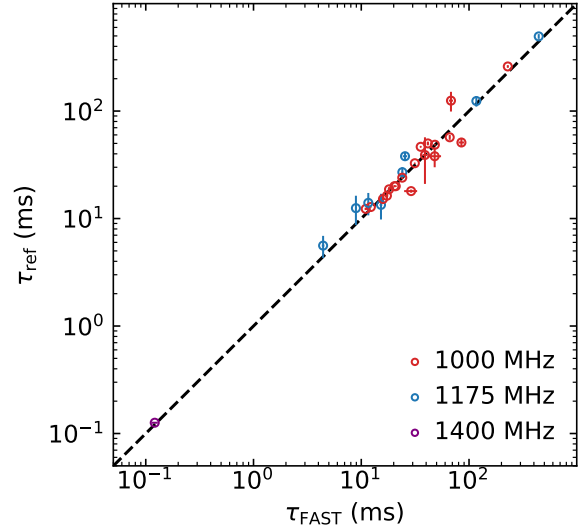


Figure 8: Comparison of pulse-broadening timescales τ measured by FAST and the values in the literature.

Many pulsars have their scattering parameters measured by Bhat et al. (2004); Nice et al. (2013); Zakharenko et al. (2013); Lewandowski et al. (2013, 2015a,b); Geyer et al. (2017); Krishnakumar et al. (2015, 2017, 2019); Oswald et al. (2021); Kravtsov et al. (2022) where observations were made at multiple frequencies. Some pulsars at specific Galactic positions also show scattering profiles (Johnston et al. 2006; Deneva et al. 2009; Bansal et al. 2019; Kirsten et al. 2019; Surnis et al. 2019; Gautam et al. 2022; Kravtsov et al. 2022; Parent et al. 2022; Sengar et al. 2023). In addition, scattering parameters have been observed for some specific pulsars, such as PSRs J0026+6320 and J2217+5733 (Surnis et al. 2019), J0534+2200 (Crab) (Kuz'min et al. 2002, 2007; Bhat et al. 2007, 2008; Oronsaye et al. 2015; Ellingson et al. 2013; Eftekhari et al. 2016; Meyers et al. 2017), J0540-6919 via giant pulse observations (Johnston & Romani 2003; Geyer et al. 2021), J0835-4510 (Vela) (Ables et al. 1970), J1208-5936 (Bernadich et al. 2023), J1227-6208 (Bernadich et al. 2024), J1410-6132 (O'Brien et al. 2008), J1550-5418 (Camilo et al. 2007), J1638-4713 (Lazarević et al. 2024), J1717-4054 (Kerr et al. 2014), J1744-2946 (Lower et al. 2024), J1745-2900 (Spitler et al. 2014; Pennucci et al. 2015), J1746-2829 (Wongpheecharuksorn et al. 2023), J1747-2809 towards the Galactic Center (Camilo et al. 2009), J1751-2737 at the Galactic Center (Bhakta et al. 2017), J1752-2806 (Xue et al. 2019), J1813-1749 near the Galactic Center (Camilo et al. 2021), J1841-0050 (Camilo et al. 2012; Wang et al. 2020), J1939+2134 (Cordes et al. 1990), J1949+3426 (Aloisi et al. 2019), J1959+2048 from giant-burst observations (Main et al. 2017), J2113+4644 (Smirnova & Shishov 2010), and J2205+6012 (Desvignes et al. 2022). After collecting all the data and discarding some uncertain values, we get the scattering parameters of 243 pulsars.

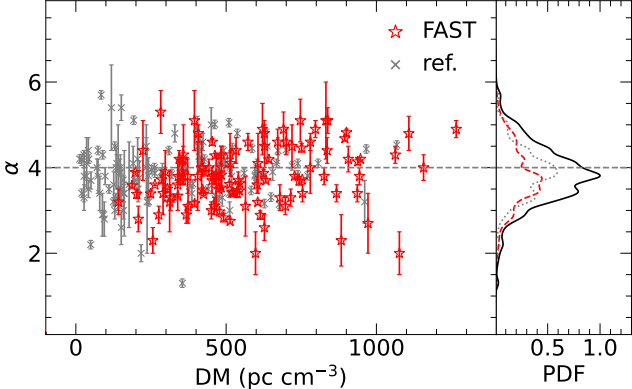


Figure 9: Distribution of scattering spectral indexes α for pulsars measured by FAST and pulsars in literature, peaked around $\alpha = 4.0$. The probability distribution function (PDF) in the right subpanel is composed by summing the Gaussian functions defined by the α and uncertainty.

Among the 122 pulsars we measured, the scattering parameters for 93 pulsars are determined for the first time, including 60 newly discovered pulsars by the FAST GPPS survey. In contrast, the scattering parameters of the other 29 pulsars have been measured previously in the literature, and they are also listed in Table 2.

Based on our measurements of τ_s in different subbands in Table A1 and the scattering spectral index α in Table 1, we interpolate the pulse-broadening timescale τ_{FAST} at the frequency specified in the literature where τ_{ref} was obtained. Then we compare the τ_{FAST} with the τ_{ref} , and find that they are in good agreement with each other, as shown in Figure 8.

Among 122 pulsars, we find that the scattering spectral indexes for 17 pulsars (including 4 pulsars with the error-bar of α greater than 0.5) have been determined previously, as listed in Table 2. The α value of PSR J1913+11025 obtained by Parent et al. (2022) is 1.6 ± 0.2 , which is very low compared with the others. We noticed that there is a possible weak component on the trailing tail in the profile of Parent et al. (2022) and also our subband profiles by the FAST. Then, we fit the profiles with an intrinsic profile with two Gaussian components and get $\alpha = 2.6 \pm 0.3$.

As mentioned in the introduction, the scattering spectral indexes could be different for different turbulent mediums, for example, $\alpha = 4.0$ for the Gaussian distribution of fluctuations, or $\alpha = 4.4$ for the general medium with a Kolmogorov spectrum (Cordes & Lazio 1991). One can find that the α values in Figure 9 have a wide distribution around 4.0, and are consistent with the results given by e.g. Lewandowski et al. (2015b) and Oswald et al. (2021). Physically, several reasons can cause the deviations of the α values: (1) the inner cutoff of the wavenumber spectrum, reducing α as low as 2 when the scattering angle is less than a critical cross-over angle (Cordes & Lazio 2003; Lewandowski et al. 2015a); (2) a low α down to 2.6 in the highly supersonic turbulence with a short-wave-dominated density spectrum (Xu & Zhang 2017); (3) a non-Kolmogorov form for the density spectrum

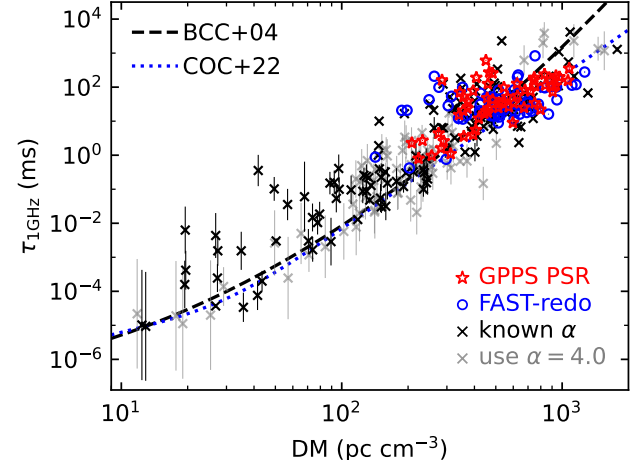


Figure 10: The distribution of the pulse-broadening timescale τ_s at 1 GHz versus pulsar DM. The values of newly discovered pulsars in the GPPS survey and the known pulsars re-detected by the FAST are specially marked by stars and circles. The other values are extrapolated from the measurements at other frequencies either by using the previously estimated α or simply assuming $\alpha = 4.0$. Two empirical relations given by Bhat et al. (2004) and Cordes et al. (2022) are outlined by a dashed line and a dotted line.

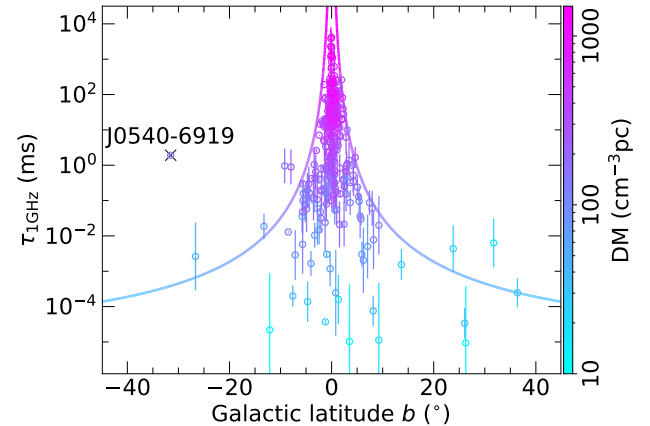


Figure 11: Pulse-broadening timescale $\tau_{1\text{GHz}}$ of pulsars at various Galactic latitudes, together with the upper limit curve calculated by the DM upper limit.

(Bhat et al. 2004); (4) a finite size of screens such as filamentary structures or clumps (Cordes & Lazio 2001); (5) the anisotropic scattering media (Brisken et al. 2010; Geyer & Karastergiou 2016).

3.2. Dependence of τ_s with DM

For analyzing the DM and direction dependence of scattering effect, all measured pulse-broadening timescales τ_s are scaled to $\tau_{1\text{GHz}}$ by using the estimated scattering spectral index α . If no observed α is available, we take $\alpha = 4.0$ for scaling τ_s . The accuracy of such extrapolated pulse-

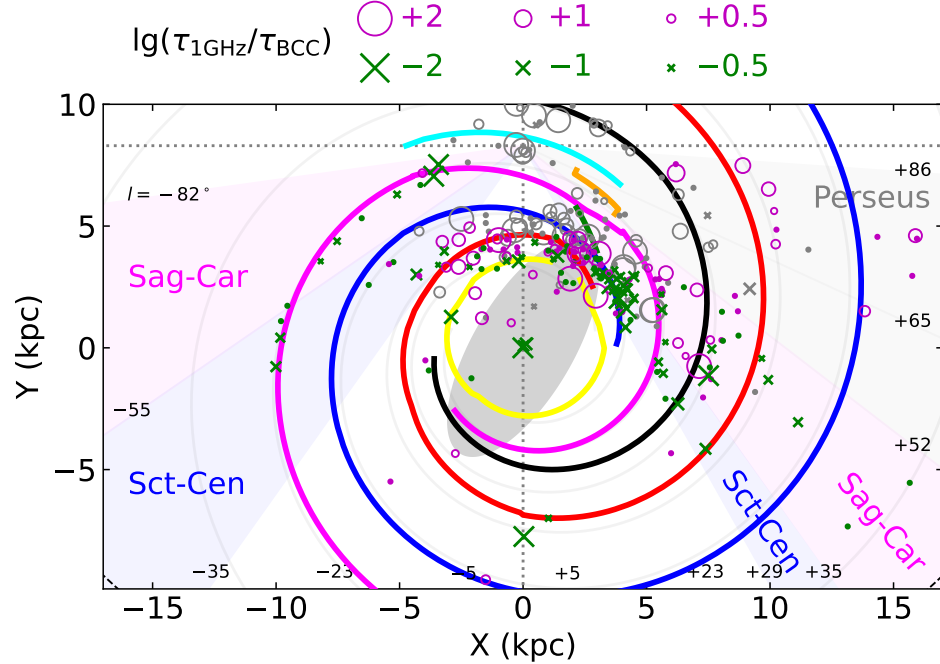


Figure 12: Distribution of scattered pulsars with $|b| < 5^\circ$ in various spiral arm regions outlined by Hou & Han (2014) and Reid et al. (2019). Crosses and circles indicate the relative $\tau_{1\text{GHz}}$ deviation from the empirical prediction given by Equation 3. Pulsars with $\text{DM} < 300 \text{ pc cm}^{-3}$ are plotted in gray. The Galactic disk is divided into and labeled with dominated spiral arms, namely the Perseus arm, the Sagittarius-Carina (Sag-Car) arm, and the Scutum-Centaurus (Sct-Cen) arm.

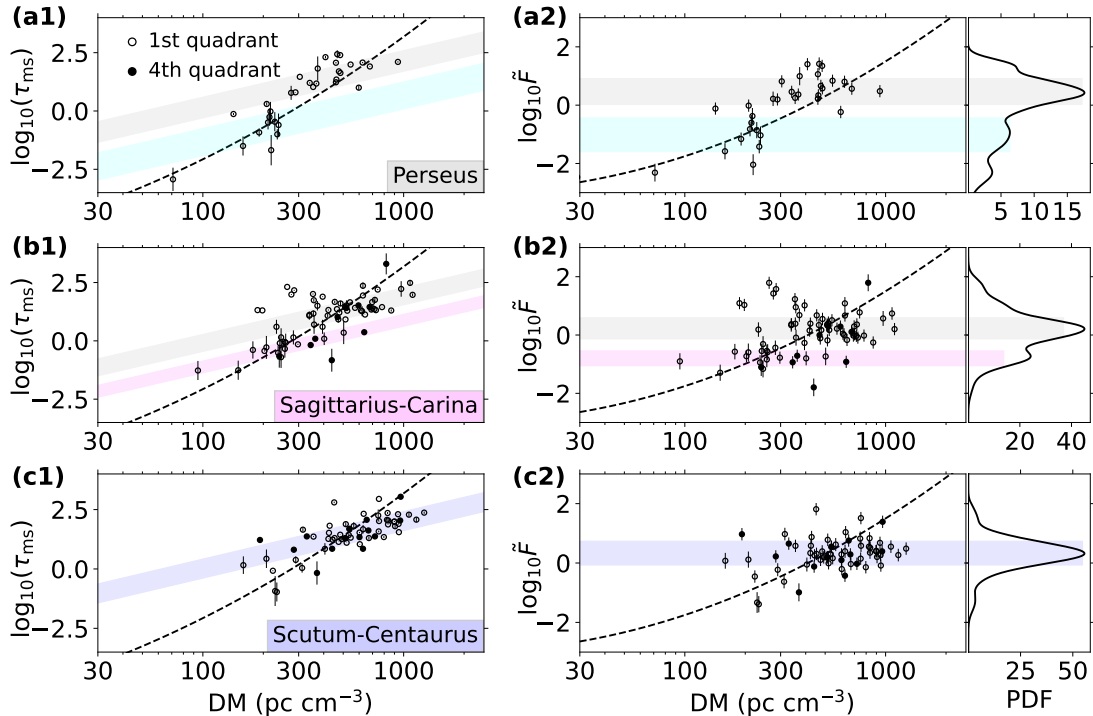


Figure 13: The pulse-broadening timescales $\tau_{1\text{GHz}}$ and the fluctuation parameter \tilde{F} for scattered pulsars in different regions dominated by different spiral arms as marked in Figure 12. The dashed line is drawn according to the empirical τ_s -DM formula in Equation 3. The probability distribution function (PDF) of \tilde{F} for pulsars in the highlighted area is expressed with the Gaussian functions in the left sub-panels. The open and filled circles label pulsars in the first and fourth Galactic quadrants.

broadening timescales rests on the uncertainty of α (Slee et al. 1980), and we take $\Delta\alpha = 0.6$ that is the standard deviation of α given by Oswald et al. (2021).

The pulse-broadening timescales $\tau_{1\text{GHz}}$ are related to the dispersion measure by an empirical formula expressed in Eq.(3) (Bhat et al. 2004; Cordes et al. 2022), as shown in Figure 10. Our new FAST measurements contribute new data at the high DMs, and are consistent with the trend.

3.3. Dependence of τ_s on the spatial distribution of the interstellar medium

The scattering effect is caused by ionized gas clouds between a pulsar and us. Therefore the pulse-broadening timescale $\tau_{1\text{GHz}}$ and the scattering spectral index α depend on the foreground clouds (e.g. Lewandowski et al. 2015a). Some low-DM pulsars show varying scattering effects (Bansal et al. 2019) because they are behind HII regions or supernova remnants (Krishnakumar et al. 2019). Here we investigate the dependence of τ_s on the spatial distribution of the interstellar medium.

First of all, the scattering effect varies with the Galactic latitude (Cordes et al. 1984; Ocker et al. 2021; Koryukova et al. 2022; He & Shi 2024). The upper limit of the pulse-broadening timescale, as shown in Figure 11, can be derived by combining the τ_s -DM relation (Equation 3) with the upper limit of the Galactic DM of $\text{DM}_{\text{max}} = (23.5 \pm 2.5) \text{ pc cm}^{-3}/\sin(b)$ (Ocker et al. 2020). Notably, the large pulse-broadening timescale of PSR J0540–6919 should be attributed to the medium in the Large Magellanic Cloud (Cordes et al. 2016).

Secondly, one may find that pulsars behind different spiral arms or HII regions show different dependence of τ_s with DM. By using the scattering parameters measured in this paper and compiled data from literature, we aim to explore the dependence of τ_s on different density fluctuations in different spiral arms (Cordes & Rickett 1998; Ocker et al. 2022)

$$\tilde{F} = (\tau_{1\text{GHz}} / 0.48 \text{ ms})(DM / 100 \text{ cm}^{-3}\text{pc})^{-2} \quad (6)$$

in different Galactic disk regions as divided in Figure 12. Here \tilde{F} is a fluctuation parameter, characterizing density fluctuations in turbulence (Cordes et al. 2016; Ocker et al. 2021). Our approach is similar to the work by Alurkar et al. (1986) and the investigations of the Sun-local region, the inner disk, and the outer disk conducted by Krishnakumar et al. (2015) and He & Shi (2024). The Galactic disk region is divided into different sections based on the Galactic longitudes. Specifically, regions dominated by the Perseus arm, the Sagittarius-Carina (Sag-Car) arm, and the Scutum-Centaurus (Scu-Cen) arm are separated, with each arm corresponding to certain ranges of Galactic longitudes.

The pulse-broadening timescales $\tau_{1\text{GHz}}$ and fluctuation parameter \tilde{F} for pulsars in these radial sectors are plotted in Figure 13(a1) to (c1) and (a2) to (c2). The fluctuation parameter \tilde{F} of different arm regions is shown in Figure 13(a2) to (c2). It is clearly shown in the figure that the data are clustered for different DM values and different values of \tilde{F} ,

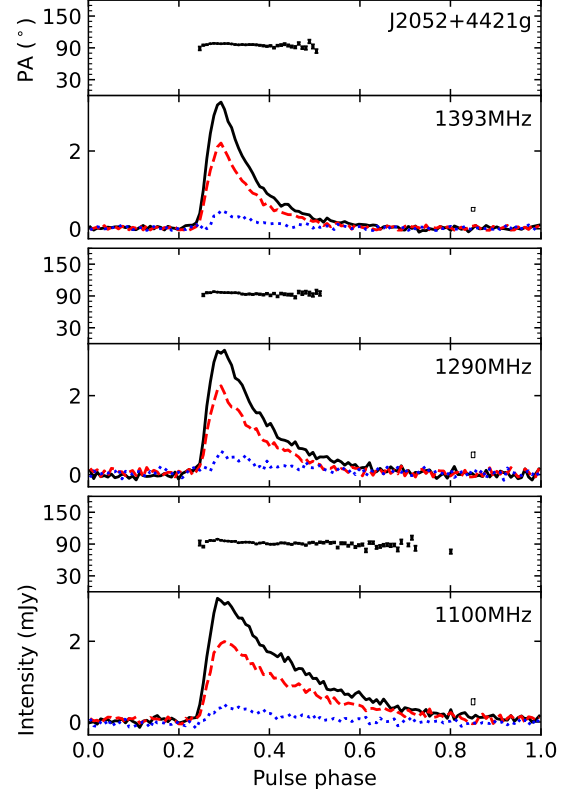


Figure 14: Polarization profiles of PSR J2052+4421g at three subbands of FAST observations. For each subband, the total intensity profile is drawn by the solid line, the linear polarization profile by the dashed line, and the circular polarization profile by the dotted line in the lower sub-panel. The box indicates the phase bin size and $\pm 1\sigma$. The polarization position angles (PAs) with error bars are shown in the top sub-panel. The polarization profiles of another 40 well-calibrated pulsars are presented in Fig. A4.

which implies that the interstellar medium in different spiral arms has different fluctuation properties. Their probability density functions (PDF) of fluctuation parameter \tilde{F} for scattered pulsars can be expressed by multiple Gaussian functions, for example, for these pulsars in the highlighted regions corresponding to spiral arms at different distances. In the Perseus Arm region there are two groups of pulsars; In the Sagittarius-Carina region there are also two groups of pulsars with different DMs and fluctuation parameters; In contrast, for Scutum-Centaurus region, only one pulsar group shows the scattering effect.

The grouping of pulsars with high fluctuations and high DMs implies that they are behind a given identifiable spiral arm. Therefore, the distances of these pulsars can be constrained as proposed in Frail & Clifton (1989); Cordes & Rickett (1998); Lazio et al. (2004). For example, the two fluctuation groups in the Perseus arm region (see Figure 13 a1-a2) should correspond to the pulsars in or behind the local arm or the pulsars in or behind the Perseus arm.

3.4. Polarization profiles

Using the DMs from the joint fitting and calibrating the FAST data, we can get the subband polarization profiles for the pulsars with strong scattering features. Polarimetric calibration of the pulse profiles has been conducted by using PSRCHIVE (van Straten 2004) following the detailed procedures given in Wang et al. (2023) (van Straten 2004). The Faraday rotation measure (RM) is obtained from the *RMFIT* in PSRCHIVE software routine. After Faraday rotation is fitted and corrected for the channel data, we get the final observed rotation measures (RM) and polarization profiles from the observation data.

Figure 14 is one example, showing the polarization profiles of PSR J2052+4421g at three subbands of FAST observations. The profiles are more extended at lower frequencies. Polarization angle curves flatten in the scattered profile tails, as discussed by Li & Han (2003). The subband polarization profiles for another 40 pulsars observed by FAST are shown in Figure A4, and their polarization parameters are listed in Table A2.

4. CONCLUSIONS

We present the pulse-broadening timescales and scattering spectral indexes for 122 pulsars derived from FAST observations at the L-band of 1.0 – 1.5 GHz. The measurements of 93 pulsars are obtained for the first time. For 29 pulsars with the scattering parameters reported in the literature, our measurements are generally consistent with previously reported values, though there are a few exceptions.

REFERENCES

- Ables, J. G., Komesaroff, M. M., & Hamilton, P. A. 1970, *Astrophys. Lett.*, 6, 147
- Aloisi, R. J., Cruz, A., Daniels, L., et al. 2019, *ApJ*, 875, 19, doi: [10.3847/1538-4357/ab0d21](https://doi.org/10.3847/1538-4357/ab0d21)
- Alurkar, S. K., Bobra, A. D., & Slee, O. B. 1986, *Australian Journal of Physics*, 39, 433, doi: [10.1071/PH860433](https://doi.org/10.1071/PH860433)
- Andersen, B. C., Fonseca, E., McKee, J. W., et al. 2023, *ApJ*, 943, 57, doi: [10.3847/1538-4357/aca485](https://doi.org/10.3847/1538-4357/aca485)
- Bansal, K., Taylor, G. B., Stovall, K., & Dowell, J. 2019, *ApJ*, 875, 146, doi: [10.3847/1538-4357/ab0d8f](https://doi.org/10.3847/1538-4357/ab0d8f)
- Bernadich, M. C. i., Balakrishnan, V., Barr, E., et al. 2023, arXiv e-prints, arXiv:2308.16802, doi: [10.48550/arXiv.2308.16802](https://doi.org/10.48550/arXiv.2308.16802)
- Bernadich, M. C. i., Venkatraman Krishnan, V., Champion, D. J., et al. 2024, arXiv e-prints, arXiv:2407.13593, doi: [10.48550/arXiv.2407.13593](https://doi.org/10.48550/arXiv.2407.13593)
- Bhakta, D., Deneva, J. S., Frail, D. A., et al. 2017, *MNRAS*, 468, 2526, doi: [10.1093/mnras/stx656](https://doi.org/10.1093/mnras/stx656)
- Bhat, N. D. R., Cordes, J. M., Camilo, F., Nice, D. J., & Lorimer, D. R. 2004, *ApJ*, 605, 759, doi: [10.1086/382680](https://doi.org/10.1086/382680)
- Bhat, N. D. R., Cordes, J. M., & Chatterjee, S. 2003, *ApJ*, 584, 782, doi: [10.1086/345775](https://doi.org/10.1086/345775)
- Bhat, N. D. R., Tingay, S. J., & Knight, H. S. 2008, *ApJ*, 676, 1200, doi: [10.1086/528735](https://doi.org/10.1086/528735)
- Bhat, N. D. R., Wayth, R. B., Knight, H. S., et al. 2007, *ApJ*, 665, 618, doi: [10.1086/519444](https://doi.org/10.1086/519444)
- Bhattacharya, D., Wijers, R. A. M. J., Hartman, J. W., & Verbunt, F. 1992, *A&A*, 254, 198
- Brisken, W. F., Macquart, J. P., Gao, J. J., et al. 2010, *ApJ*, 708, 232, doi: [10.1088/0004-637X/708/1/232](https://doi.org/10.1088/0004-637X/708/1/232)
- Camilo, F., Ransom, S. M., Chatterjee, S., Johnston, S., & Demorest, P. 2012, *ApJ*, 746, 63, doi: [10.1088/0004-637X/746/1/63](https://doi.org/10.1088/0004-637X/746/1/63)
- Camilo, F., Ransom, S. M., Gaensler, B. M., & Lorimer, D. R. 2009, *ApJL*, 700, L34, doi: [10.1088/0004-637X/700/1/L34](https://doi.org/10.1088/0004-637X/700/1/L34)
- Camilo, F., Ransom, S. M., Halpern, J. P., & Reynolds, J. 2007, *ApJL*, 666, L93, doi: [10.1086/521826](https://doi.org/10.1086/521826)
- Camilo, F., Ransom, S. M., Halpern, J. P., & Roshi, D. A. 2021, *ApJ*, 917, 67, doi: [10.3847/1538-4357/ac0720](https://doi.org/10.3847/1538-4357/ac0720)
- Champion, D. J., Ransom, S. M., Lazarus, P., et al. 2008, *Science*, 320, 1309, doi: [10.1126/science.1157580](https://doi.org/10.1126/science.1157580)

We find that aligning the front edge of the subband profiles at the half or quarter of the profile peak can yield better DM values for most pulsars than those obtainable using *PDMP*. However, the best DM value can be determined by aligning the main peak of the modeled intrinsic profiles obtained from joint fitting the scattered subband profiles.

We find that in the regions with spiral arms, the pulsars could be grouped by their DM values and the relative fluctuations, which indicate the density irregularities in the spiral arm regions. On the other hand, the grouping of pulsars can probably be a rough indication of pulsar locations.

From the FAST observations, the polarized profiles have been obtained for 41 pulsars with scattered profiles at three subbands, which constantly show the flattened polarization angle curves in the scattered profile tails, as suggested by Li & Han (2003).

ACKNOWLEDGEMENTS

We thank the referee, Prof. Ramesh Bhat, for very careful reading and helpful suggestions. The authors are supported by the Natural Science Foundation of China: No. 11988101 and 11833009, the National SKA Program of China (2020SKA0120100) and the Chinese Academy of Sciences via the project JZHKYPT-2021-06. FAST is a Chinese national mega-science facility, built and operated by the National Astronomical Observatories, Chinese Academy of Sciences. We all appreciate the excellent performance of the FAST and the operation team.

- Chen, X., Han, J. L., Su, W. Q., Yang, Z. L., & Zhou, D. J. 2023a, Research in Astronomy and Astrophysics, 23, 104004, doi: [10.1088/1674-4527/acd52b](https://doi.org/10.1088/1674-4527/acd52b)
- Chen, X., Yan, Y., Han, J. L., et al. 2023b, Nature Astronomy, 7, 1235, doi: [10.1038/s41550-023-02056-z](https://doi.org/10.1038/s41550-023-02056-z)
- Cordes, J. M., Ananthakrishnan, S., & Dennison, B. 1984, Nature, 309, 689, doi: [10.1038/309689a0](https://doi.org/10.1038/309689a0)
- Cordes, J. M., & Lazio, T. J. 1991, ApJ, 376, 123, doi: [10.1086/170261](https://doi.org/10.1086/170261)
- Cordes, J. M., & Lazio, T. J. W. 1997, ApJ, 475, 557, doi: [10.1086/303569](https://doi.org/10.1086/303569)
- . 2001, ApJ, 549, 997, doi: [10.1086/319442](https://doi.org/10.1086/319442)
- Cordes, J. M., & Lazio, T. J. W. 2002, arXiv e-prints, astro. <https://arxiv.org/abs/astro-ph/0207156>
- . 2003, arXiv e-prints, astro. <https://arxiv.org/abs/astro-ph/0301598>
- Cordes, J. M., Ocker, S. K., & Chatterjee, S. 2022, ApJ, 931, 88, doi: [10.3847/1538-4357/ac6873](https://doi.org/10.3847/1538-4357/ac6873)
- Cordes, J. M., & Rickett, B. J. 1998, ApJ, 507, 846, doi: [10.1086/306358](https://doi.org/10.1086/306358)
- Cordes, J. M., Weisberg, J. M., & Boriakoff, V. 1985, ApJ, 288, 221, doi: [10.1086/162784](https://doi.org/10.1086/162784)
- Cordes, J. M., Wharton, R. S., Spitler, L. G., Chatterjee, S., & Wasserman, I. 2016, arXiv e-prints, arXiv:1605.05890. <https://arxiv.org/abs/1605.05890>
- Cordes, J. M., Wolszczan, A., Dewey, R. J., Blaskiewicz, M., & Stinebring, D. R. 1990, ApJ, 349, 245, doi: [10.1086/168310](https://doi.org/10.1086/168310)
- Cronyn, W. M. 1970, Science, 168, 1453, doi: [10.1126/science.168.3938.1453](https://doi.org/10.1126/science.168.3938.1453)
- Demorest, P. B. 2011, MNRAS, 416, 2821, doi: [10.1111/j.1365-2966.2011.19230.x](https://doi.org/10.1111/j.1365-2966.2011.19230.x)
- Deneva, J. S., Cordes, J. M., & Lazio, T. J. W. 2009, ApJL, 702, L177, doi: [10.1088/0004-637X/702/2/L177](https://doi.org/10.1088/0004-637X/702/2/L177)
- Desvignes, G., Cognard, I., Smith, D. A., et al. 2022, A&A, 667, A79, doi: [10.1051/0004-6361/202244171](https://doi.org/10.1051/0004-6361/202244171)
- Dexter, J., Deller, A., Bower, G. C., et al. 2017, MNRAS, 471, 3563, doi: [10.1093/mnras/stx1777](https://doi.org/10.1093/mnras/stx1777)
- Eftekhari, T., Stovall, K., Dowell, J., Schinzel, F. K., & Taylor, G. B. 2016, ApJ, 829, 62, doi: [10.3847/0004-637X/829/2/62](https://doi.org/10.3847/0004-637X/829/2/62)
- Ellingson, S. W., Clarke, T. E., Craig, J., et al. 2013, ApJ, 768, 136, doi: [10.1088/0004-637X/768/2/136](https://doi.org/10.1088/0004-637X/768/2/136)
- Fonseca, E., Pleunis, Z., Breitman, D., et al. 2024, ApJS, 271, 49, doi: [10.3847/1538-4365/ad27d6](https://doi.org/10.3847/1538-4365/ad27d6)
- Frail, D. A., & Clifton, T. R. 1989, ApJ, 336, 854, doi: [10.1086/167056](https://doi.org/10.1086/167056)
- Gautam, T., Ridolfi, A., Freire, P. C. C., et al. 2022, A&A, 664, A54, doi: [10.1051/0004-6361/202243062](https://doi.org/10.1051/0004-6361/202243062)
- Geyer, M., & Karastergiou, A. 2016, MNRAS, 462, 2587, doi: [10.1093/mnras/stw1724](https://doi.org/10.1093/mnras/stw1724)
- Geyer, M., Karastergiou, A., Kondratiev, V. I., et al. 2017, MNRAS, 470, 2659, doi: [10.1093/mnras/stx1151](https://doi.org/10.1093/mnras/stx1151)
- Geyer, M., Serylak, M., Abbatte, F., et al. 2021, MNRAS, 505, 4468, doi: [10.1093/mnras/stab1501](https://doi.org/10.1093/mnras/stab1501)
- Han, J. L., Wang, C., Wang, P. F., et al. 2021, Research in Astronomy and Astrophysics, 21, 107, doi: [10.1088/1674-4527/21/5/107](https://doi.org/10.1088/1674-4527/21/5/107)
- Han, J. L., Zhou, D. J., Wang, C., et al. 2024, Research in Astronomy and Astrophysics, submitted
- He, Q., & Shi, X. 2024, MNRAS, 527, 5183, doi: [10.1093/mnras/stad3561](https://doi.org/10.1093/mnras/stad3561)
- He, Q., Shi, X., & Li, G. 2025, arXiv e-prints, arXiv:2502.09158. <https://arxiv.org/abs/2502.09158>
- Hessels, J. W. T., Spitler, L. G., Seymour, A. D., et al. 2019, ApJL, 876, L23, doi: [10.3847/2041-8213/ab13ae](https://doi.org/10.3847/2041-8213/ab13ae)
- Hotan, A. W., van Straten, W., & Manchester, R. N. 2004, PASA, 21, 302, doi: [10.1071/AS04022](https://doi.org/10.1071/AS04022)
- Hou, L. G., & Han, J. L. 2014, A&A, 569, A125, doi: [10.1051/0004-6361/201424039](https://doi.org/10.1051/0004-6361/201424039)
- Jiang, P., Tang, N.-Y., Hou, L.-G., et al. 2020, Research in Astronomy and Astrophysics, 20, 064, doi: [10.1088/1674-4527/20/5/64](https://doi.org/10.1088/1674-4527/20/5/64)
- Jing, W. C., Han, J. L., Hong, T., et al. 2023, MNRAS, 523, 4949, doi: [10.1093/mnras/stad1782](https://doi.org/10.1093/mnras/stad1782)
- Johnston, S., Kramer, M., Lorimer, D. R., et al. 2006, MNRAS, 373, L6, doi: [10.1111/j.1745-3933.2006.00232.x](https://doi.org/10.1111/j.1745-3933.2006.00232.x)
- Johnston, S., & Romani, R. W. 2003, ApJL, 590, L95, doi: [10.1086/376826](https://doi.org/10.1086/376826)
- Karastergiou, A. 2009, MNRAS, 392, L60, doi: [10.1111/j.1745-3933.2008.00585.x](https://doi.org/10.1111/j.1745-3933.2008.00585.x)
- Kerr, M., Hobbs, G., Shannon, R. M., et al. 2014, MNRAS, 445, 320, doi: [10.1093/mnras/stu1716](https://doi.org/10.1093/mnras/stu1716)
- Kirsten, F., Bhat, N. D. R., Meyers, B. W., et al. 2019, ApJ, 874, 179, doi: [10.3847/1538-4357/ab0c05](https://doi.org/10.3847/1538-4357/ab0c05)
- Komesaroff, M. M., Hamilton, P. A., & Ables, J. G. 1972, Australian Journal of Physics, 25, 759, doi: [10.1071/PH720759](https://doi.org/10.1071/PH720759)
- Koryukova, T. A., Pushkarev, A. B., Plavin, A. V., & Kovalev, Y. Y. 2022, MNRAS, 515, 1736, doi: [10.1093/mnras/stac1898](https://doi.org/10.1093/mnras/stac1898)
- Kramer, M. 1994, A&AS, 107, 527
- Kravtsov, I. P., Zakharenko, V. V., Ulyanov, O. M., et al. 2022, MNRAS, 512, 4324, doi: [10.1093/mnras/stab3369](https://doi.org/10.1093/mnras/stab3369)
- Krishnakumar, M. A., Joshi, B. C., & Manoharan, P. K. 2017, ApJ, 846, 104, doi: [10.3847/1538-4357/aa7af2](https://doi.org/10.3847/1538-4357/aa7af2)
- Krishnakumar, M. A., Maan, Y., Joshi, B. C., & Manoharan, P. K. 2019, ApJ, 878, 130, doi: [10.3847/1538-4357/ab20c5](https://doi.org/10.3847/1538-4357/ab20c5)
- Krishnakumar, M. A., Mitra, D., Naidu, A., Joshi, B. C., & Manoharan, P. K. 2015, ApJ, 804, 23, doi: [10.1088/0004-637X/804/1/23](https://doi.org/10.1088/0004-637X/804/1/23)
- Kuz'min, A. D., & Izvekova, V. A. 1993, MNRAS, 260, 724, doi: [10.1093/mnras/260.4.724](https://doi.org/10.1093/mnras/260.4.724)

- Kuz'min, A. D., Kondrat'ev, V. I., Kostyuk, S. V., et al. 2002, *Astronomy Letters*, 28, 251, doi: [10.1134/1.1467260](https://doi.org/10.1134/1.1467260)
- Kuz'min, A. D., Losovskii, B. Y., & Lapaev, K. A. 2007, *Astronomy Reports*, 51, 615, doi: [10.1134/S1063772907080021](https://doi.org/10.1134/S1063772907080021)
- Kuzmin, A. D., & Losovsky, B. Y. 2007, *Astronomical and Astrophysical Transactions*, 26, 597, doi: [10.1080/10556790701610282](https://doi.org/10.1080/10556790701610282)
- Lazarević, S., Filipović, M. D., Dai, S., et al. 2024, *PASA*, 41, e032, doi: [10.1017/pasa.2024.13](https://doi.org/10.1017/pasa.2024.13)
- Lazio, T. J. W., Cordes, J. M., de Bruyn, A. G., & Macquart, J. P. 2004, *NewAR*, 48, 1439, doi: [10.1016/j.newar.2004.09.039](https://doi.org/10.1016/j.newar.2004.09.039)
- Lee, L. C., & Jokipii, J. R. 1975a, *ApJ*, 196, 695, doi: [10.1086/153458](https://doi.org/10.1086/153458)
- . 1975b, *ApJ*, 201, 532, doi: [10.1086/153916](https://doi.org/10.1086/153916)
- Lewandowski, W., Dembska, M., Kijak, J., & Kowalińska, M. 2013, *MNRAS*, 434, 69, doi: [10.1093/mnras/stt989](https://doi.org/10.1093/mnras/stt989)
- Lewandowski, W., Kowalińska, M., & Kijak, J. 2015a, *MNRAS*, 449, 1570, doi: [10.1093/mnras/stv385](https://doi.org/10.1093/mnras/stv385)
- Lewandowski, W., Rożko, K., Kijak, J., Bhattacharyya, B., & Roy, J. 2015b, *MNRAS*, 454, 2517, doi: [10.1093/mnras/stv2159](https://doi.org/10.1093/mnras/stv2159)
- Li, X. H., & Han, J. L. 2003, *A&A*, 410, 253, doi: [10.1051/0004-6361:20031190](https://doi.org/10.1051/0004-6361:20031190)
- Löhmer, O., Kramer, M., Mitra, D., Lorimer, D. R., & Lyne, A. G. 2001, *ApJL*, 562, L157, doi: [10.1086/338324](https://doi.org/10.1086/338324)
- Löhmer, O., Mitra, D., Gupta, Y., Kramer, M., & Ahuja, A. 2004, *A&A*, 425, 569, doi: [10.1051/0004-6361:20035881](https://doi.org/10.1051/0004-6361:20035881)
- Lower, M. E., Dai, S., Johnston, S., & Barr, E. D. 2024, *ApJL*, 967, L16, doi: [10.3847/2041-8213/ad4866](https://doi.org/10.3847/2041-8213/ad4866)
- Main, R., van Kerkwijk, M., Pen, U.-L., Mahajan, N., & Vanderlinde, K. 2017, *ApJL*, 840, L15, doi: [10.3847/2041-8213/aa6f03](https://doi.org/10.3847/2041-8213/aa6f03)
- Manchester, R. N., Hobbs, G. B., Teoh, A., & Hobbs, M. 2005, *AJ*, 129, 1993, doi: [10.1086/428488](https://doi.org/10.1086/428488)
- Meyers, B. W., Tremblay, S. E., Bhat, N. D. R., et al. 2017, *ApJ*, 851, 20, doi: [10.3847/1538-4357/aa8bba](https://doi.org/10.3847/1538-4357/aa8bba)
- Nan, R. 2006, *Science in China: Physics, Mechanics and Astronomy*, 49, 129, doi: [10.1007/s11433-006-0129-9](https://doi.org/10.1007/s11433-006-0129-9)
- Nan, R., Li, D., Jin, C., et al. 2011, *International Journal of Modern Physics D*, 20, 989, doi: [10.1142/S0218271811019335](https://doi.org/10.1142/S0218271811019335)
- Nice, D. J., Altiere, E., Bogdanov, S., et al. 2013, *ApJ*, 772, 50, doi: [10.1088/0004-637X/772/1/50](https://doi.org/10.1088/0004-637X/772/1/50)
- O'Brien, J. T., Johnston, S., Kramer, M., et al. 2008, *MNRAS*, 388, L1, doi: [10.1111/j.1745-3933.2008.00481.x](https://doi.org/10.1111/j.1745-3933.2008.00481.x)
- Ocker, S. K., Cordes, J. M., & Chatterjee, S. 2020, *ApJ*, 897, 124, doi: [10.3847/1538-4357/ab98f9](https://doi.org/10.3847/1538-4357/ab98f9)
- . 2021, *ApJ*, 911, 102, doi: [10.3847/1538-4357/abeb6e](https://doi.org/10.3847/1538-4357/abeb6e)
- Ocker, S. K., Cordes, J. M., Chatterjee, S., & Gorsuch, M. R. 2022, arXiv e-prints, arXiv:2203.16716. <https://arxiv.org/abs/2203.16716>
- Oronsaye, S. I., Ord, S. M., Bhat, N. D. R., et al. 2015, *ApJ*, 809, 51, doi: [10.1088/0004-637X/809/1/51](https://doi.org/10.1088/0004-637X/809/1/51)
- Oswald, L. S., Karastergiou, A., Posselt, B., et al. 2021, *MNRAS*, 504, 1115, doi: [10.1093/mnras/stab980](https://doi.org/10.1093/mnras/stab980)
- Parent, E., Sewalls, H., Freire, P. C. C., et al. 2022, *ApJ*, 924, 135, doi: [10.3847/1538-4357/ac375d](https://doi.org/10.3847/1538-4357/ac375d)
- Pennucci, T. T., Possenti, A., Esposito, P., et al. 2015, *ApJ*, 808, 81, doi: [10.1088/0004-637X/808/1/81](https://doi.org/10.1088/0004-637X/808/1/81)
- Ramachandran, R., Mitra, D., Deshpande, A. A., McConnell, D. M., & Ables, J. G. 1997, *MNRAS*, 290, 260, doi: [10.1093/mnras/290.2.260](https://doi.org/10.1093/mnras/290.2.260)
- Reid, M. J., Menten, K. M., Brunthaler, A., et al. 2019, *ApJ*, 885, 131, doi: [10.3847/1538-4357/ab4a11](https://doi.org/10.3847/1538-4357/ab4a11)
- Rickett, B. J. 1977, *ARA&A*, 15, 479, doi: [10.1146/annurev.aa.15.090177.002403](https://doi.org/10.1146/annurev.aa.15.090177.002403)
- . 1990, *ARA&A*, 28, 561, doi: [10.1146/annurev.aa.28.090190.003021](https://doi.org/10.1146/annurev.aa.28.090190.003021)
- Scheuer, P. A. G. 1968, *Nature*, 218, 920, doi: [10.1038/218920a0](https://doi.org/10.1038/218920a0)
- Sengar, R., Bailes, M., Balakrishnan, V., et al. 2023, *MNRAS*, 522, 1071, doi: [10.1093/mnras/stad508](https://doi.org/10.1093/mnras/stad508)
- Singha, J., Joshi, B. C., Krishnakumar, M. A., et al. 2024, *MNRAS*, 535, 1184, doi: [10.1093/mnras/stae2405](https://doi.org/10.1093/mnras/stae2405)
- Slee, O. B., Dulk, G. A., & Otrupcek, R. E. 1980, *PASA*, 4, 100, doi: [10.1017/S1323358000018968](https://doi.org/10.1017/S1323358000018968)
- Smirnova, T. V., & Shishov, V. I. 2010, *Astronomy Reports*, 54, 139, doi: [10.1134/S106377291002006X](https://doi.org/10.1134/S106377291002006X)
- Spitler, L. G., Lee, K. J., Eatough, R. P., et al. 2014, *ApJL*, 780, L3, doi: [10.1088/2041-8205/780/1/L3](https://doi.org/10.1088/2041-8205/780/1/L3)
- Staelin, D. H. 1970, *Nature*, 226, 69, doi: [10.1038/226069a0](https://doi.org/10.1038/226069a0)
- Su, W. Q., Han, J. L., Wang, P. F., et al. 2023, arXiv e-prints, arXiv:2305.16754, doi: [10.48550/arXiv.2305.16754](https://doi.org/10.48550/arXiv.2305.16754)
- Surnis, M. P., Joshi, B. C., McLaughlin, M. A., et al. 2019, *ApJ*, 870, 8, doi: [10.3847/1538-4357/aaee7f](https://doi.org/10.3847/1538-4357/aaee7f)
- Sutton, J. M. 1971, *MNRAS*, 155, 51, doi: [10.1093/mnras/155.1.51](https://doi.org/10.1093/mnras/155.1.51)
- Taylor, J. H., & Cordes, J. M. 1993, *ApJ*, 411, 674, doi: [10.1086/172870](https://doi.org/10.1086/172870)
- van Straten, W. 2004, *ApJS*, 152, 129, doi: [10.1086/383187](https://doi.org/10.1086/383187)
- van Straten, W., & Bailes, M. 2011, *PASA*, 28, 1, doi: [10.1071/AS10021](https://doi.org/10.1071/AS10021)
- van Straten, W., Demorest, P., & Oslowski, S. 2012, *Astronomical Research and Technology*, 9, 237, doi: [10.48550/arXiv.1205.6276](https://doi.org/10.48550/arXiv.1205.6276)
- Voûte, J. L. L., Kouwenhoven, M. L. A., van Haren, P. C., et al. 2002, *A&A*, 385, 733, doi: [10.1051/0004-6361:20020123](https://doi.org/10.1051/0004-6361:20020123)
- Wang, P. F., Han, J. L., Xu, J., et al. 2023, *Research in Astronomy and Astrophysics*, 23, 104002, doi: [10.1088/1674-4527/aceaf1](https://doi.org/10.1088/1674-4527/aceaf1)
- Wang, S. Q., Wang, J. B., Hobbs, G., et al. 2020, *ApJ*, 897, 8, doi: [10.3847/1538-4357/ab9302](https://doi.org/10.3847/1538-4357/ab9302)

- Wongphechauxsorn, J., Champion, D. J., Bailes, M., et al. 2023, arXiv e-prints, arXiv:2310.14008,
doi: [10.48550/arXiv.2310.14008](https://doi.org/10.48550/arXiv.2310.14008)
- Xu, J., Han, J., Wang, P., & Yan, Y. 2022, Science China Physics, Mechanics, and Astronomy, 65, 129704,
doi: [10.1007/s11433-022-2033-2](https://doi.org/10.1007/s11433-022-2033-2)
- Xu, S., & Zhang, B. 2017, ApJ, 835, 2,
doi: [10.3847/1538-4357/835/1/2](https://doi.org/10.3847/1538-4357/835/1/2)
- Xue, M., Ord, S. M., Tremblay, S. E., et al. 2019, PASA, 36, e025,
doi: [10.1017/pasa.2019.19](https://doi.org/10.1017/pasa.2019.19)
- Yan, Y., Han, J. L., Zhou, D. J., et al. 2024, ApJ, 965, 25,
doi: [10.3847/1538-4357/ad2e9c](https://doi.org/10.3847/1538-4357/ad2e9c)
- Yan, Y., Wang, P. F., & Han, J. L. 2023, MNRAS, 523, 5207,
doi: [10.1093/mnras/stad1775](https://doi.org/10.1093/mnras/stad1775)
- Yao, J. M., Manchester, R. N., & Wang, N. 2017, ApJ, 835, 29,
doi: [10.3847/1538-4357/835/1/29](https://doi.org/10.3847/1538-4357/835/1/29)
- Young, O., & Lam, M. T. 2024, ApJ, 962, 131,
doi: [10.3847/1538-4357/ad1ce7](https://doi.org/10.3847/1538-4357/ad1ce7)
- Zakharenko, V. V., Vasylyeva, I. Y., Konovalenko, A. A., et al. 2013, MNRAS, 431, 3624, doi: [10.1093/mnras/stt470](https://doi.org/10.1093/mnras/stt470)

APPENDIX

This appendix presents big databases, including two long tables and figures.

The FAST observations were carried out in the band of 1.0-1.5 GHz, with various RFI in different frequency channels for different pulsars at different times. Considering these various RFI situations, we measured the pulse-broadening timescales at these sub-bands, and published them directly in Table A1.

Figure A1 presents the scattering profiles in 3-5 subbands for 118 pulsars which have been well-fitted in the joint model-fitting to subband profiles, except for PSR J1844-0310 and J1850-0026, which probably have frequency-evolution for intrinsic profile components and are presented in Figure A2.

The polarized subband profiles for 41 scattered pulsars are presented in Figure A4. The polarization parameters are given in Table A2.

Table A 1: Pulse-broadening timescales τ_s measured for subband profiles from FAST observations. The FAST observation band is divided into 3 – 5 subbands according to the RFI situation so that the central frequencies of subbands differ from pulsar to pulsar and are given in the table.

PSR Name	$\tau_s @ \nu_1$ (ms@MHz)	$\tau_s @ \nu_2$ (ms@MHz)	$\tau_s @ \nu_3$ (ms@MHz)	$\tau_s @ \nu_4$ (ms@MHz)	$\tau_s @ \nu_5$ (ms@MHz)
J1833–0204g	0.5±0.1@1105	0.4±0.1@1259	0.2±0.1@1399		
J1841–0157	10.29±0.09@1085	7.4±0.1@1182	4.83±0.08@1337	4.0±0.1@1420	
J1842–0153	23.7±0.2@1092	17.8±0.1@1183	11.70±0.09@1319	8.5±0.1@1420	
J1842–0258g	17.2±0.7@1085	12.1±0.5@1190	7.6±0.3@1319	4.6±0.4@1421	
J1842–0309	53±3@1084	45±2@1187	31±1@1320	21±0@1421	
J1843–0050	15.0±0.3@1072	12.7±0.3@1121	6.9±0.2@1351	5.5±0.3@1432	
J1843–0137	20.2±0.3@1084	14.5±0.3@1174	9.1±0.1@1329	6.9±0.1@1418	
J1843–0157g	85±7@1093	62±5@1174	44±1@1323	32±1@1420	
J1844–0030	8.5±0.2@1086	6.5±0.2@1176	4.3±0.2@1334	3.6±0.2@1420	
J1844–0136g	46±3@1085	33±2@1187	22±1@1317	14±1@1421	
J1844–0142g	16.3±0.8@1085	13±0@1172	7.8±0.4@1323	5.6±0.4@1419	
J1844–0202g	33±5@1095	26±4@1288	12±1@1398		
J1844–0240	46±7@1096	35±3@1331	19±2@1421		
J1844–0244	14.3±0.3@1087	11.0±0.3@1180	8.1±0.2@1321	6.6±0.2@1420	
J1844–0256	67±12@1085	51±5@1179	35±2@1326	23±1@1418	
J1844–0302	17.4±0.8@1077	11.2±0.8@1188	7.6±0.5@1328	5.9±0.5@1420	
J1844–0310	52±2@1056	48±2@1119	29±1@1237	23.8±0.6@1328	16.8±0.4@1418
J1845–0103g	25±2@1085	17±1@1179	10.0±0.5@1323	7.1±0.4@1420	
J1845–0142g	307±194@1077	34±4@1187	26±2@1318	16±1@1421	
J1845–0144g	158±5@1086	105±4@1172	66±1@1326	53±1@1420	
J1845–0229Ag	118±9@1094	85±3@1334	35±1@1420		
J1845–0229Bg	61±8@1278	68±13@1324	43±4@1375		
J1845–0243g	284 ⁺⁴⁸⁴ ₋₁₁₉ @1106	69±10@1258	45±4@1400		
J1845–0254g	168 ⁺⁵² ₋₃₃ @1342	153±29@1385	184±36@1430		
J1845–0316	15.7±0.7@1077	10.4±0.5@1183	6.6±0.4@1326	4.6±0.3@1420	
J1846–0211g	84±7@1086	43±3@1191	25±2@1319	20±2@1421	
J1848–0055	109 ⁺³⁷ ₋₂₂ @1086	69±9@1171	37±2@1317	32±1@1420	
J1849–0013	55±1@1085	38.0±0.8@1181	27.0±0.4@1325	21.5±0.3@1420	
J1849–0040	152±21@1083	99±10@1198	72±4@1320	51±1@1420	
J1849–0200g	962±498@1086	245 ⁺¹⁷⁷ ₋₆₅ @1174	117±9@1331	87±4@1421	
J1850+0242	14±5@1347	12±6@1377	7 ⁺⁹ ₋₃ @1408		
J1850–0002	31±1@1077	24±1@1177	13.8±0.8@1330	11.5±0.8@1419	
J1850–0006	176±3@1085	132±2@1180	86±1@1315	61±1@1420	
J1850–0020	23±0@1085	14±0@1183	10.4±0.9@1324	9.7±0.9@1420	
J1850–0026	27.3±0.4@1072	21.6±0.2@1122	14.1±0.1@1239	10.81±0.08@1332	8.15±0.06@1421
J1850–0031	67±1@1084	50.2±0.9@1184	32.5±0.4@1323	22.7±0.3@1421	
J1850–0050g	73±9@1241	54±2@1316	43±1@1370	36±1@1432	
J1851+0233	198 ⁺²⁰³ ₋₈₈ @1095	29±5@1257	21±2@1401		
J1851–0029	9.7±0.1@1085	7.1±0.1@1186	4.6±0.1@1330	3.86±0.08@1420	
J1851–0108g	15±1@1086	9±1@1140	6.4±0.4@1334		
J1851–0241	80±10@1078	50±5@1186	29±2@1318	28±1@1420	
J1852+0013	16.6±0.2@1085	12.4±0.2@1182	9.1±0.1@1322	7.9±0.1@1421	
J1852+0018	14.4±0.7@1086	11.8±0.6@1184	6.7±0.4@1321	5.5±0.3@1420	
J1852+0031	635±2@1085	462±1@1175	286.4±0.5@1324	215.8±0.5@1420	
J1852+0056g	74±3@1086	49±1@1183	31.8±0.8@1321	22.3±0.7@1420	
J1852+0309g	2 ⁺⁵ ₋₁ @1117	1.1±0.2@1223	0.9±0.1@1356		
J1852–0127	49±1@1072	43±1@1120	25±0@1273	19.7±0.3@1349	
J1853+0237g	54±7@1099	25±2@1274	18±1@1399		
J1853+0505	145±0@1088	120.5±0.8@1169	76.6±0.5@1319	56.3±0.5@1420	
J1853+0545	14.7±0.1@1087	11.62±0.08@1157	7.13±0.03@1319	5.44±0.03@1420	
J1853–0049g	4 ⁺³ ₋₁ @1092	2.6±0.4@1247	1.8±0.2@1360		
J1853–0054g	11±0@1086	9.0±0.6@1177	6.2±0.4@1325	3.3±0.3@1420	
J1854+0131g	496±39@1077	542±42@1129	237±10@1336	199±7@1423	
J1854–00	14.0±0.5@1077	9.9±0.5@1190	7.1±0.5@1322	5.5±0.4@1421	
J1855+0205	17±1@1086	8.7±0.8@1186	7.1±0.5@1315	5.2±0.4@1420	
J1855+0422	33.3±0.7@1084	21.9±0.6@1187	13.8±0.4@1333	11.2±0.4@1419	
J1855+0455g	16±2@1076	11±1@1181	6.7±0.7@1315	5±1@1421	
J1855+0511g	116±4@1079	77±2@1186	59±1@1318	42±2@1419	
J1855+0527	73±3@1086	55±2@1178	32±1@1320	24±1@1420	

... to be continued.

Table A 1: – *continued*

PSR Name	$\tau_s @ \nu_1$ (ms@MHz)	$\tau_s @ \nu_2$ (ms@MHz)	$\tau_s @ \nu_3$ (ms@MHz)	$\tau_s @ \nu_4$ (ms@MHz)	$\tau_s @ \nu_5$ (ms@MHz)
J1855–0221g	0.58±0.06@1098	0.29±0.03@1259	0.16±0.01@1399		
J1856+0245	17 ⁺⁵ ₋₃ @1084	14 ⁺¹⁰ ₋₂ @1187	6±1@1317	1±1@1420	
J1857+0143	32±1@1086	23.5±0.7@1187	16.9±0.4@1313	12.6±0.3@1420	
J1857+0210	20±1@1082	14±0@1170	7.1±0.6@1322	5.8±0.5@1419	
J1857+0214	119±22@1216	80±6@1379	80±6@1406		
J1857+0300	18±3@1070	13±1@1103	2±1@1391		
J1857+0526	17.2±0.2@1087	12.4±0.1@1183	8.36±0.07@1317	6.37±0.06@1418	
J1858+0215	32±1@1085	25±2@1183	17±1@1319	9±1@1421	
J1858+0244g	1.2±0.2@1098	0.46±0.04@1262	0.30±0.02@1399		
J1859+0430	16±2@1087	12±1@1184	9.3±0.8@1317	5±1@1419	
J1859+0601	70±3@1086	63±2@1187	39±1@1320	30±1@1421	
J1900+0438	196 ⁺¹⁸⁷ ₋₅₈ @1108	68±5@1265	37±2@1399		
J1901+0459	72±7@1087	51±6@1173	28±2@1336	26±2@1420	
J1902–0107g	1.3±0.3@1103	1.0±0.2@1263	0.5±0.1@1397		
J1903+0327	0.43±0.02@1104	0.16±0.01@1341	0.12±0.01@1422		
J1905+0600	14.7±0.3@1086	10.0±0.2@1184	6.5±0.1@1312	5.1±0.2@1421	
J1907+0534	14.9±0.4@1087	11.0±0.4@1187	8.4±0.3@1319	6.4±0.3@1420	
J1908+0833	17±1@1104	13±1@1269	8.0±0.7@1399		
J1908+0839	6.9±0.1@1087	5.7±0.1@1183	4.24±0.08@1320	3.59±0.07@1419	
J1908+0909	6.11±0.09@1086	4.96±0.07@1185	4.15±0.05@1312	3.69±0.06@1421	
J1910+0534	11.7±0.3@1085	9.1±0.4@1170	5.8±0.3@1321	4.0±0.4@1422	
J1910+1026	17±1@1080	12±1@1188	9.4±0.6@1318	7.0±0.5@1420	
J1911+0101A	0.36±0.02@1084	0.29±0.02@1188	0.28±0.02@1320	0.25±0.02@1420	
J1911+0925	32±6@1087	22±3@1180	14±1@1314	12±2@1419	
J1913+1000	14.4±0.4@1072	11.2±0.6@1121	10±1@1246	5.8 ^{+0.7} _{-0.9} @1355	
J1913+1102	8.4±0.3@1078	5.4±0.1@1185	3.61±0.06@1317	2.58±0.03@1421	
J1913+11025	66±4@1069	71±5@1119	35±2@1348	37±2@1426	
J1913+1145	10.0±0.2@1087	7.7±0.1@1181	5.12±0.09@1330	4.05±0.07@1420	
J1914+1054g	7±1@1085	6±1@1168	3.6±0.6@1320	3.5±0.5@1420	
J1916+0844	9.50±0.08@1085	7.34±0.08@1174	4.60±0.07@1321	3.37±0.06@1420	
J1918+1340g	20±1@1085	12±1@1167	7.4±0.4@1320	6.3±0.5@1420	
J1919+1314	15.3±0.5@1087	11.0±0.6@1166	7.2±0.3@1328	6.4±0.3@1420	
J1919+1341	1.2±0.1@1085	0.77±0.08@1185	0.63±0.05@1319	0.45±0.07@1421	
J1920+1110	14.9±0.2@1087	10.7±0.2@1187	7.1±0.1@1317	5.3±0.2@1420	
J1920+1340g	270±63@1088	236±23@1275	230±21@1383		
J1921+1216g	0.59±0.05@1098	0.41±0.03@1262	0.30±0.01@1400		
J1921+1259g	41±2@1077	16±2@1169	13±1@1321	10±1@1422	
J1921+1340g	103±3@1061	53±2@1235	42.2±0.8@1328	32.5±0.7@1421	
J1921+1505g	14±1@1086	8±1@1188	3±1@1314	3±1@1420	
J1922+1512g	59±1@1085	45±1@1182	33.1±0.8@1318	24±0@1421	
J1924+1713	30±1@1086	21±1@1182	13.7±0.7@1330	10.3±0.6@1422	
J1928+1923	35.4±0.4@1084	27.3±0.4@1172	16.4±0.3@1333	11.7±0.2@1420	
J1946+2433g	3 ⁺⁷ ₋₁ @1124	1.8±0.4@1267	1.2±0.3@1375		
J1946+2757g	89±5@1086	68±7@1159	40±2@1336	34±2@1421	
J1950+2414	0.57±0.05@1086	0.44±0.06@1160	0.29±0.03@1333	0.25±0.02@1419	
J1959+3141g	13.7±0.8@1085	8.4±0.5@1186	5.3±0.5@1318	4.7±0.5@1421	
J2004+3429	7.7±0.1@1084	5.5±0.1@1181	3.50±0.06@1329	2.74±0.04@1421	
J2005+3411g	31.1±0.6@1085	22.0±0.6@1173	14.3±0.3@1328	10.6±0.3@1421	
J2015+3404g	1.4±0.2@1106	0.82±0.07@1263	0.65±0.04@1400		
J2019+3718g	16.3±0.4@1072	13.6±0.3@1149	9.6±0.2@1248	7.9±0.1@1348	6.3±0.1@1433
J2021+3651	13±1@1085	8.0±0.8@1171	6.4±0.5@1327	5.0±0.4@1421	
J2021+4024g	59±2@1086	48±1@1171	29±0@1328	24.0±0.6@1421	
J2022+3845g	171±7@1085	133±6@1171	65±2@1333	56±1@1422	
J2030+3818g	7±1@1076	6±1@1122	5±2@1301	3±0@1352	
J2030+3944g	98±6@1087	63±3@1180	47±1@1318	32±0@1422	
J2032+4055g	71 ⁺⁹⁶ ₋₃₂ @1109	21±2@1252	12.8±0.8@1397		
J2041+3934g	126±13@1073	160±18@1146	84±15@1198	66±3@1353	
J2041+46	22.9±0.1@1085	16.95±0.09@1173	11.61±0.05@1318	9.36±0.05@1420	
J2045+4431g	21±4@1096	26 ⁺¹² ₋₇ @1284	17±2@1399		
J2046+4236g	311 ⁺⁴⁶⁸ ₋₁₁₃ @1146	87±7@1343	67±5@1421		
J2046+4253g	98±5@1086	61±2@1183	38.8±0.9@1321	30.6±0.6@1422	
J2052+4421g	71±1@1087	56.7±0.7@1174	35.4±0.4@1330	27.4±0.3@1419	
J2057+4557g	35±0@1085	28±0@1174	15.9±0.3@1320	13.5±0.3@1413	

... ended.

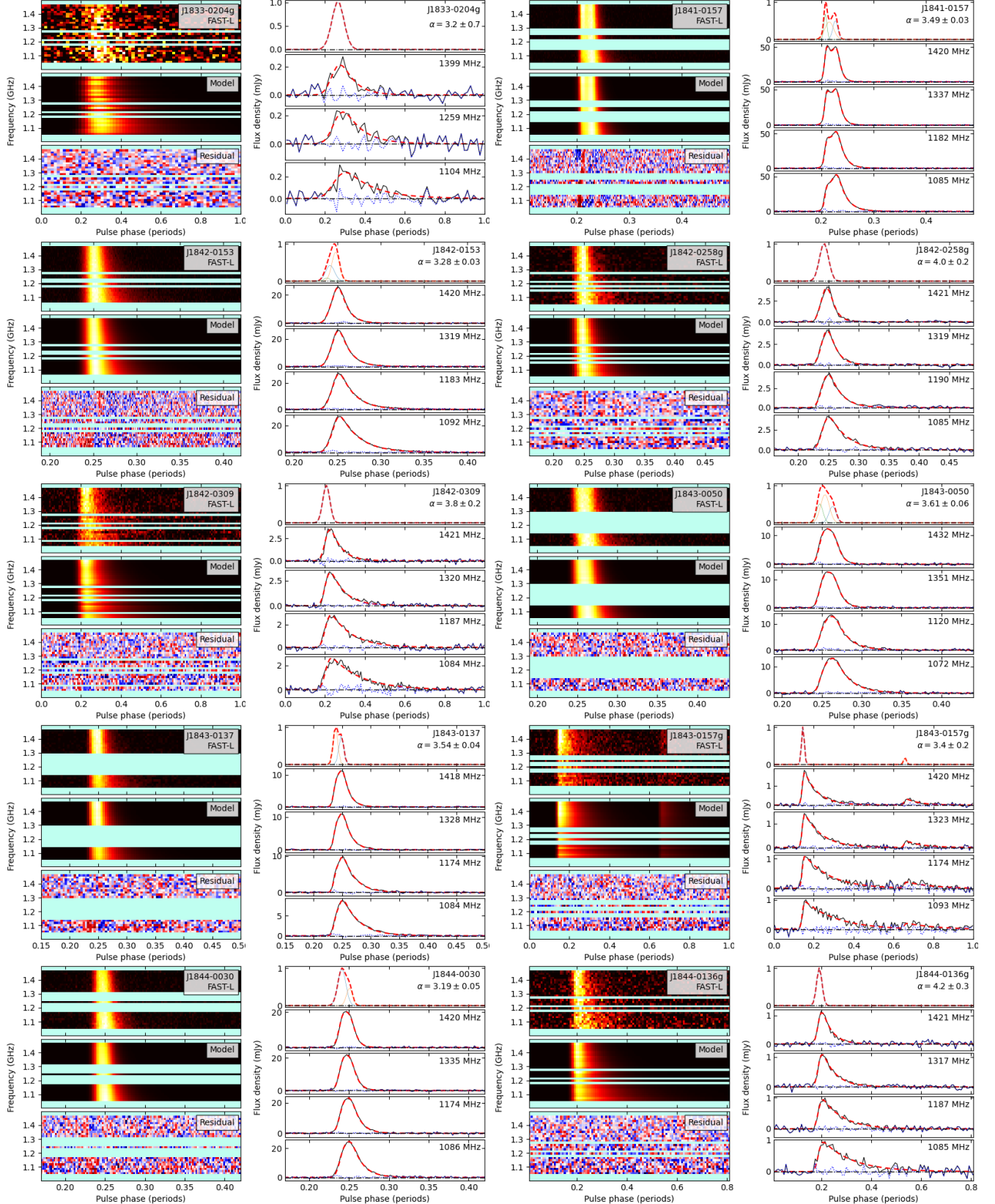


Figure A 1: The observed and modeled scattering profiles for 120 pulsars. Comparing the phase-time waterfall 2D intensity plot for the 32 channels in the FAST observation band (left top) with the modeled scattered profiles (left middle), one can get the residual plot (left bottom). The intrinsic profiles and the modeled subband profiles are given on the right

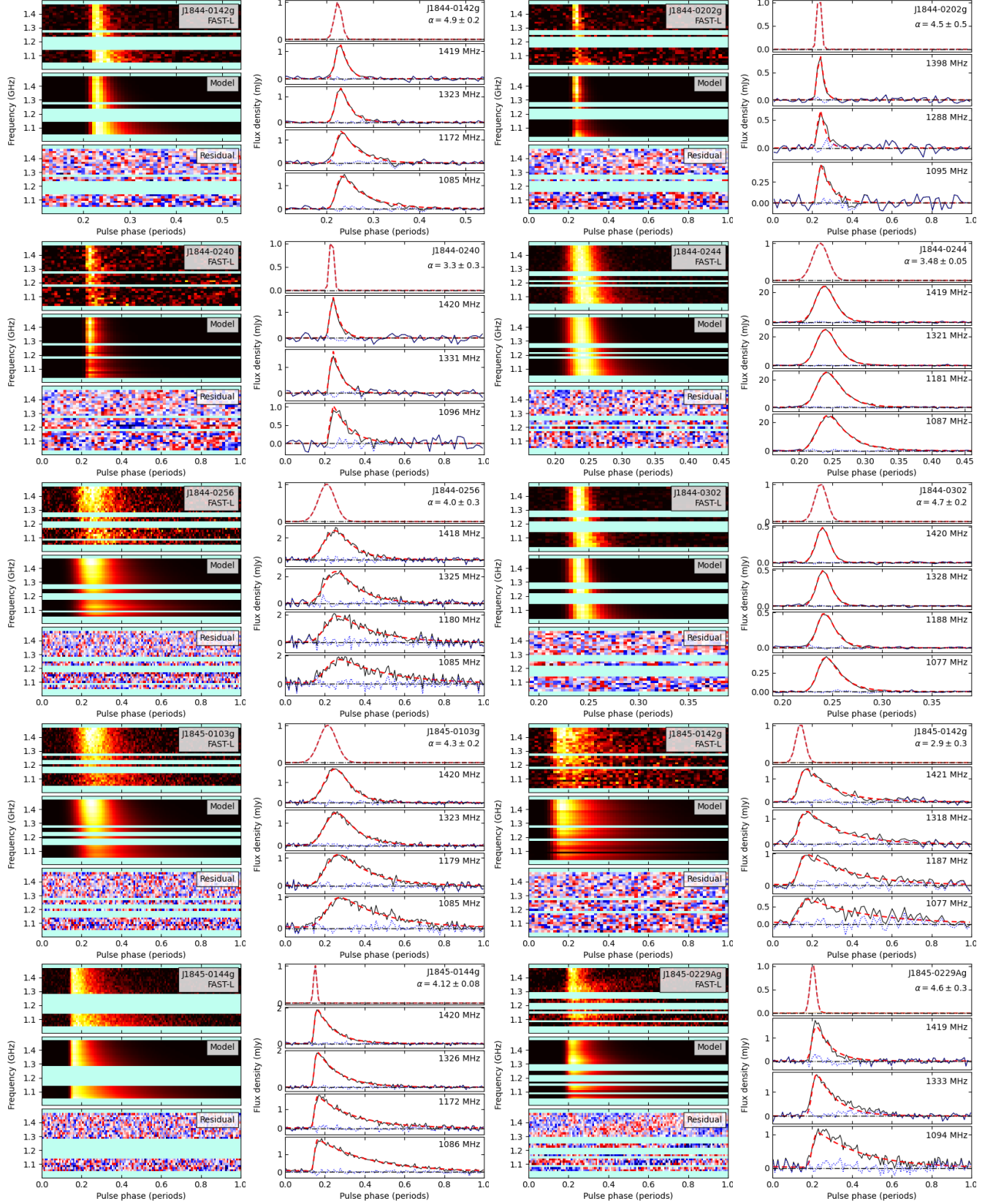


Figure A 1: — to be continued.

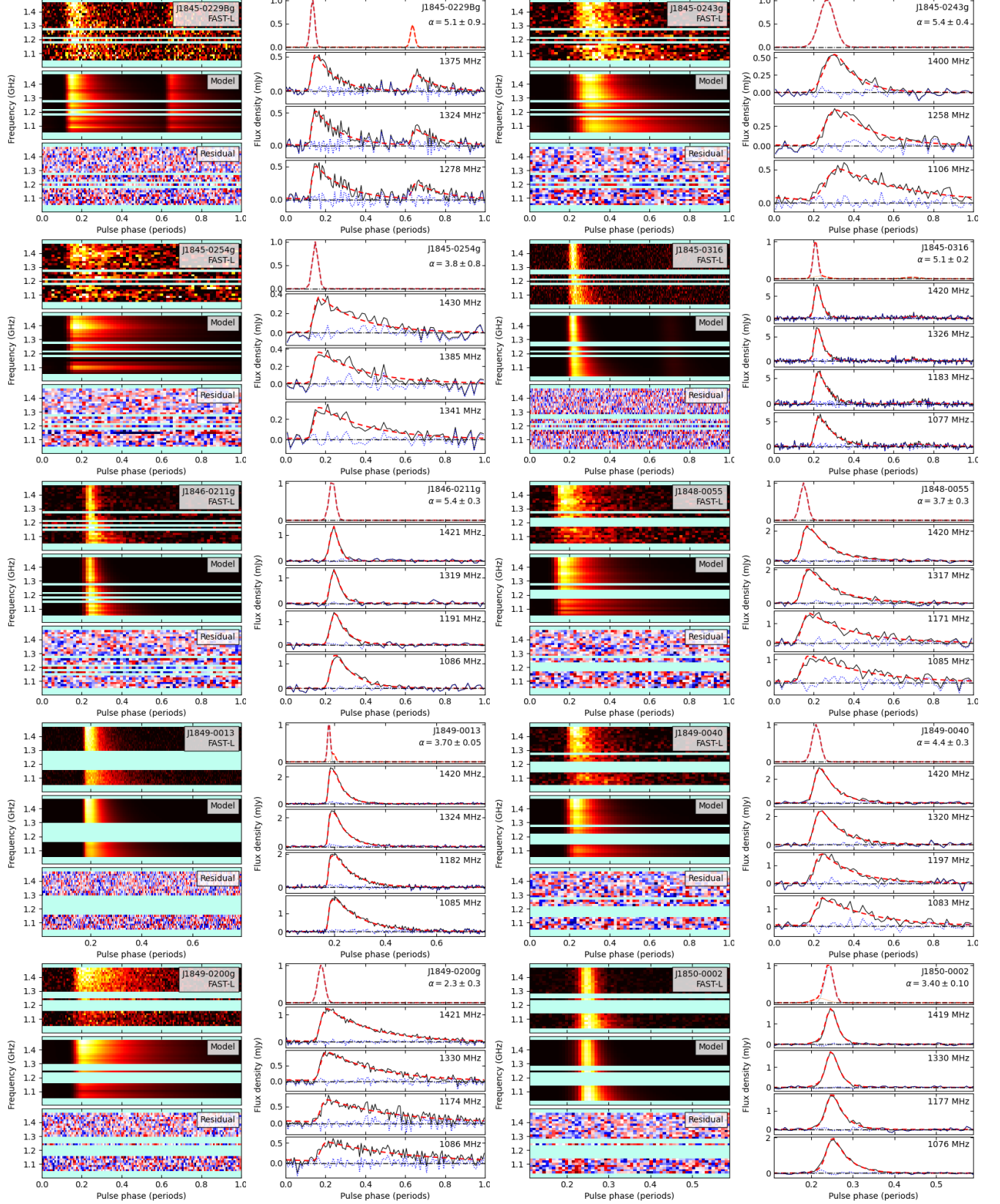


Figure A 1: — to be continued.

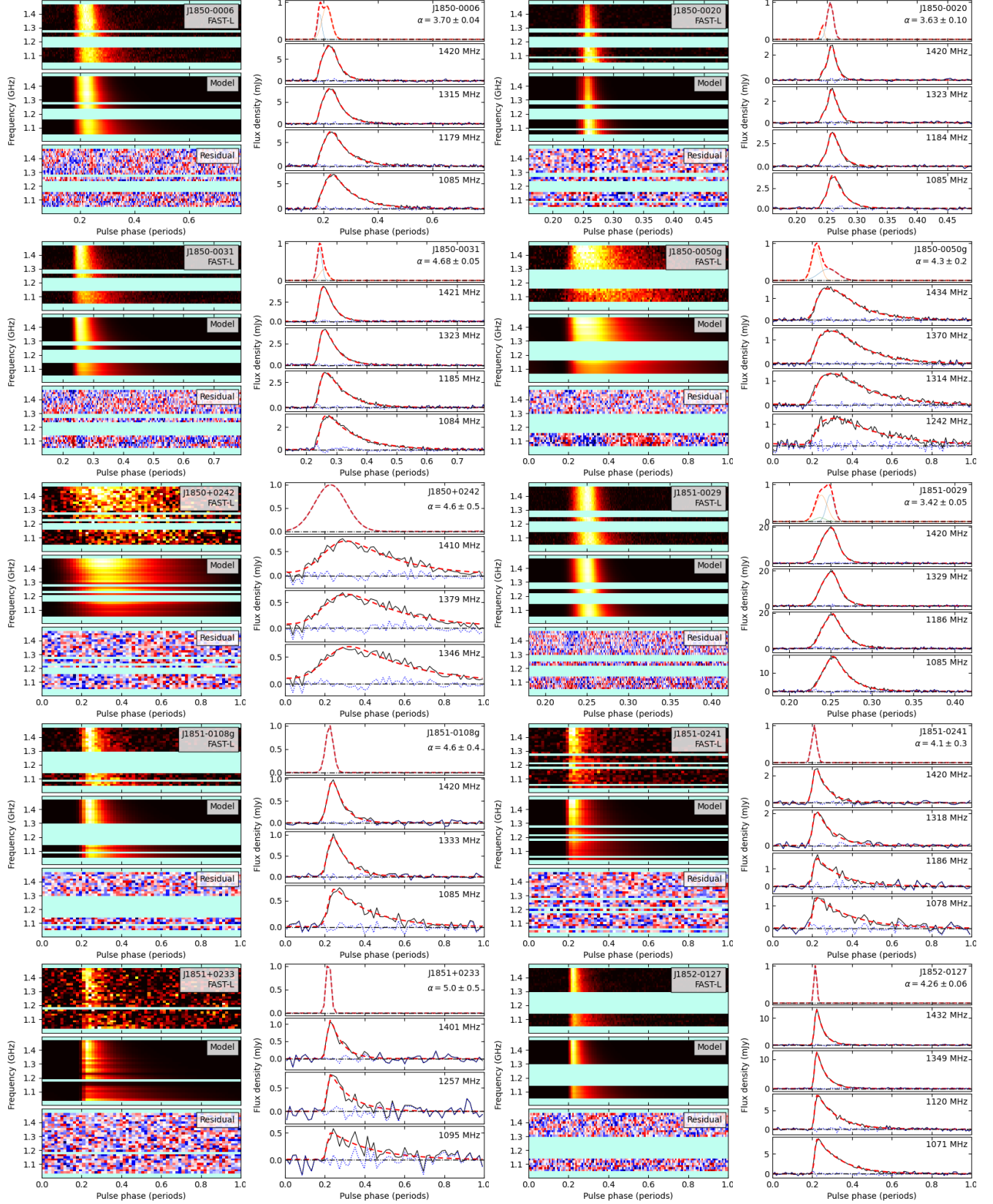


Figure A 1: — to be continued.

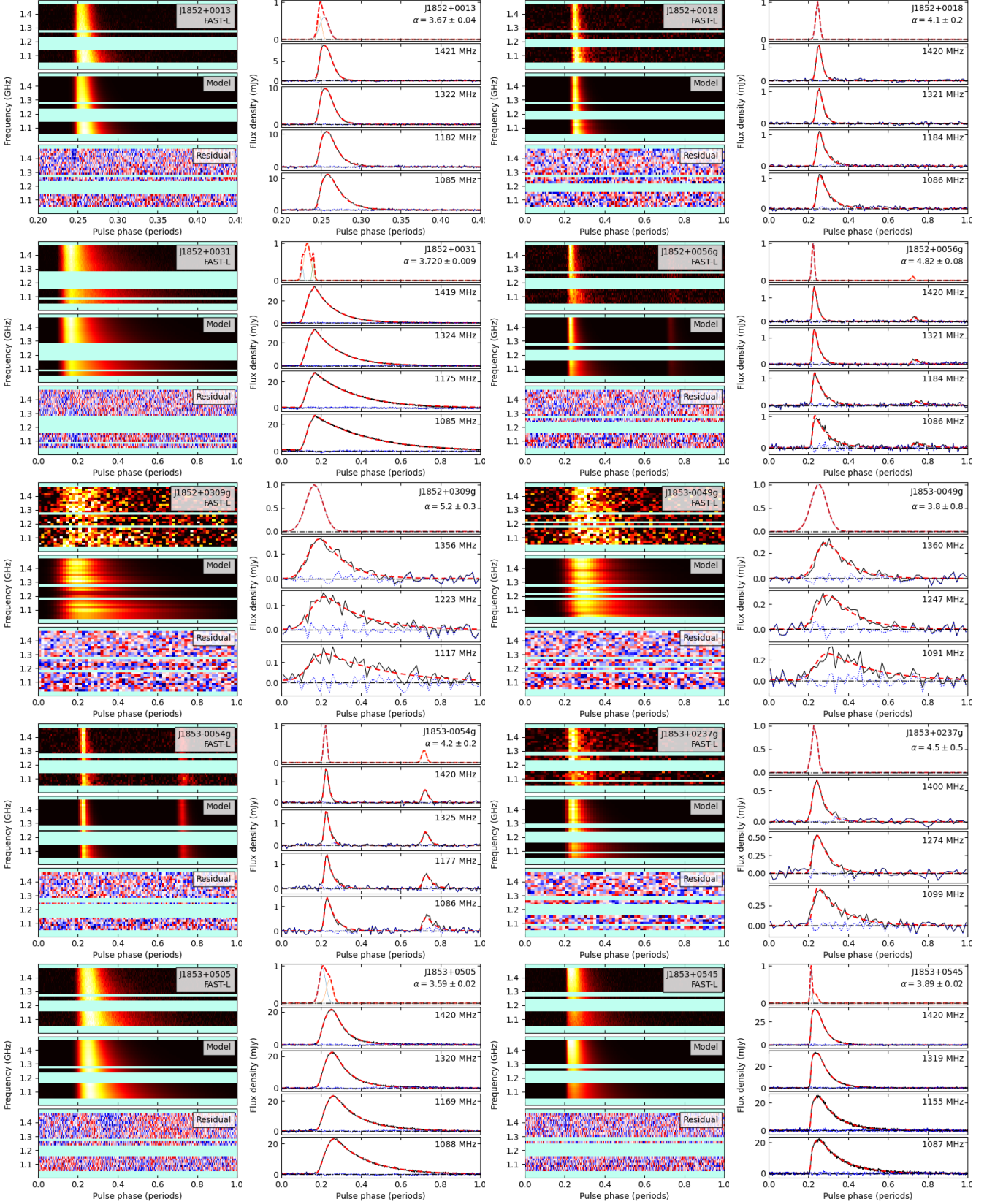


Figure A 1: — to be continued.

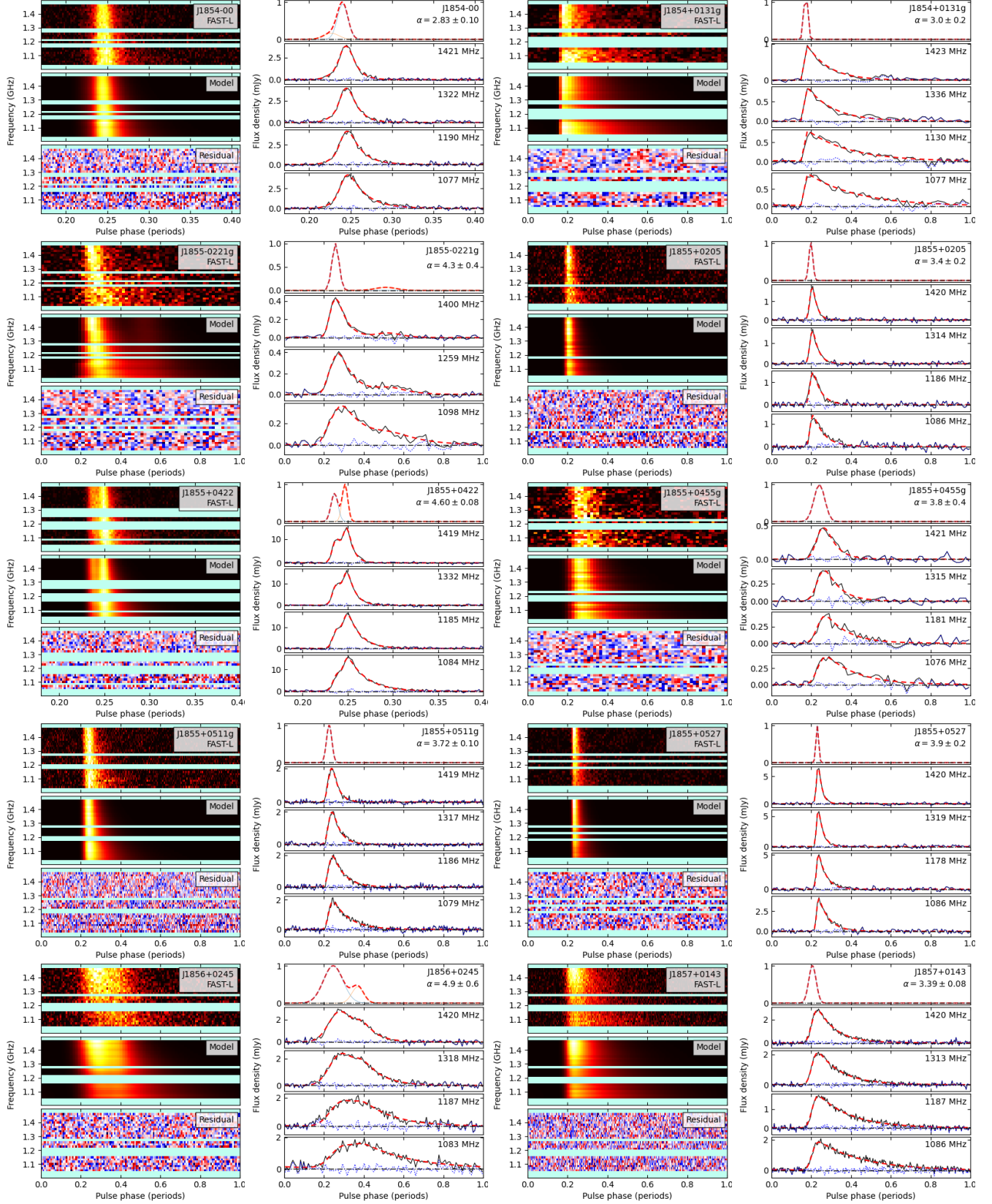


Figure A 1: — to be continued.

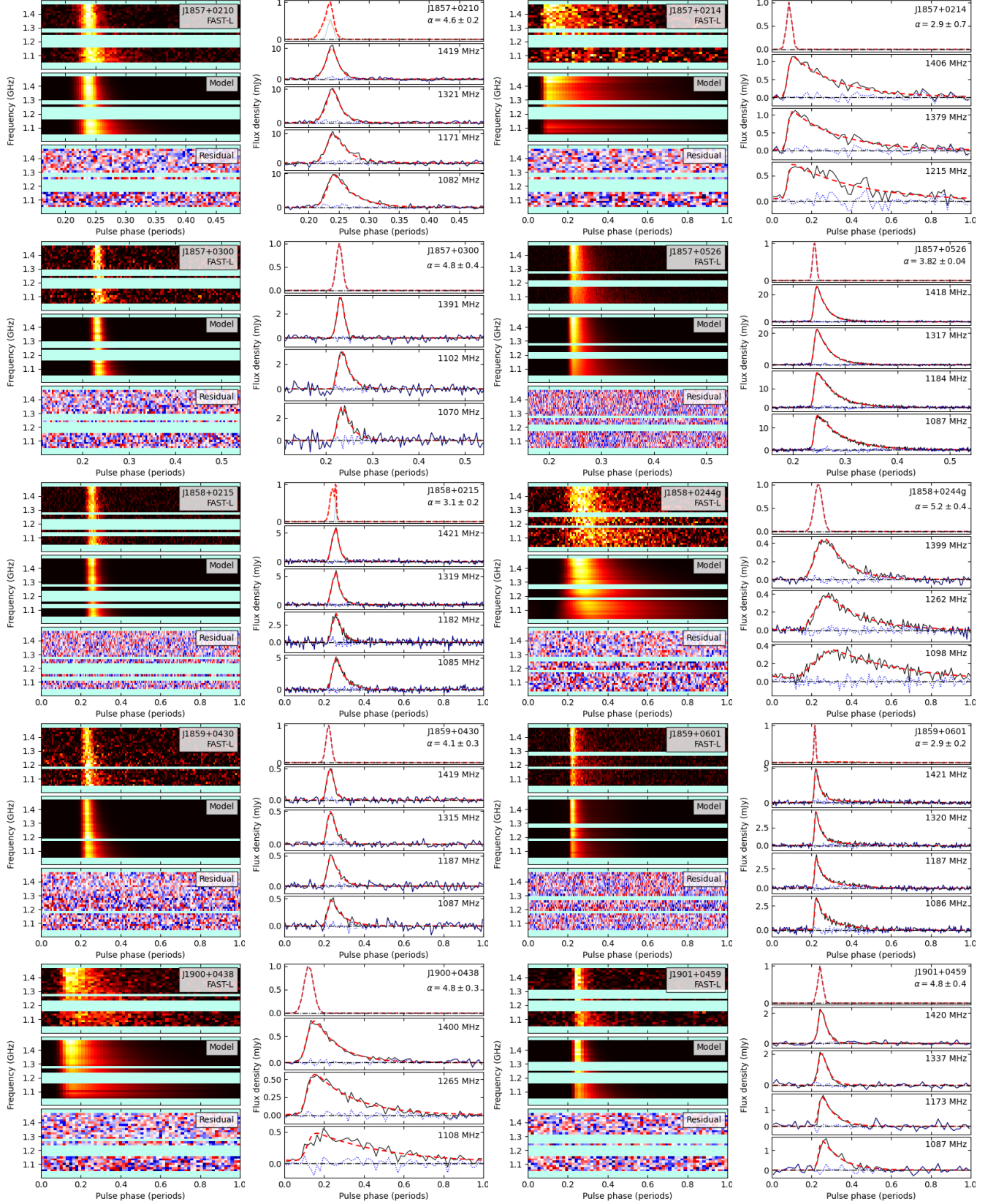


Figure A 1: — to be continued.

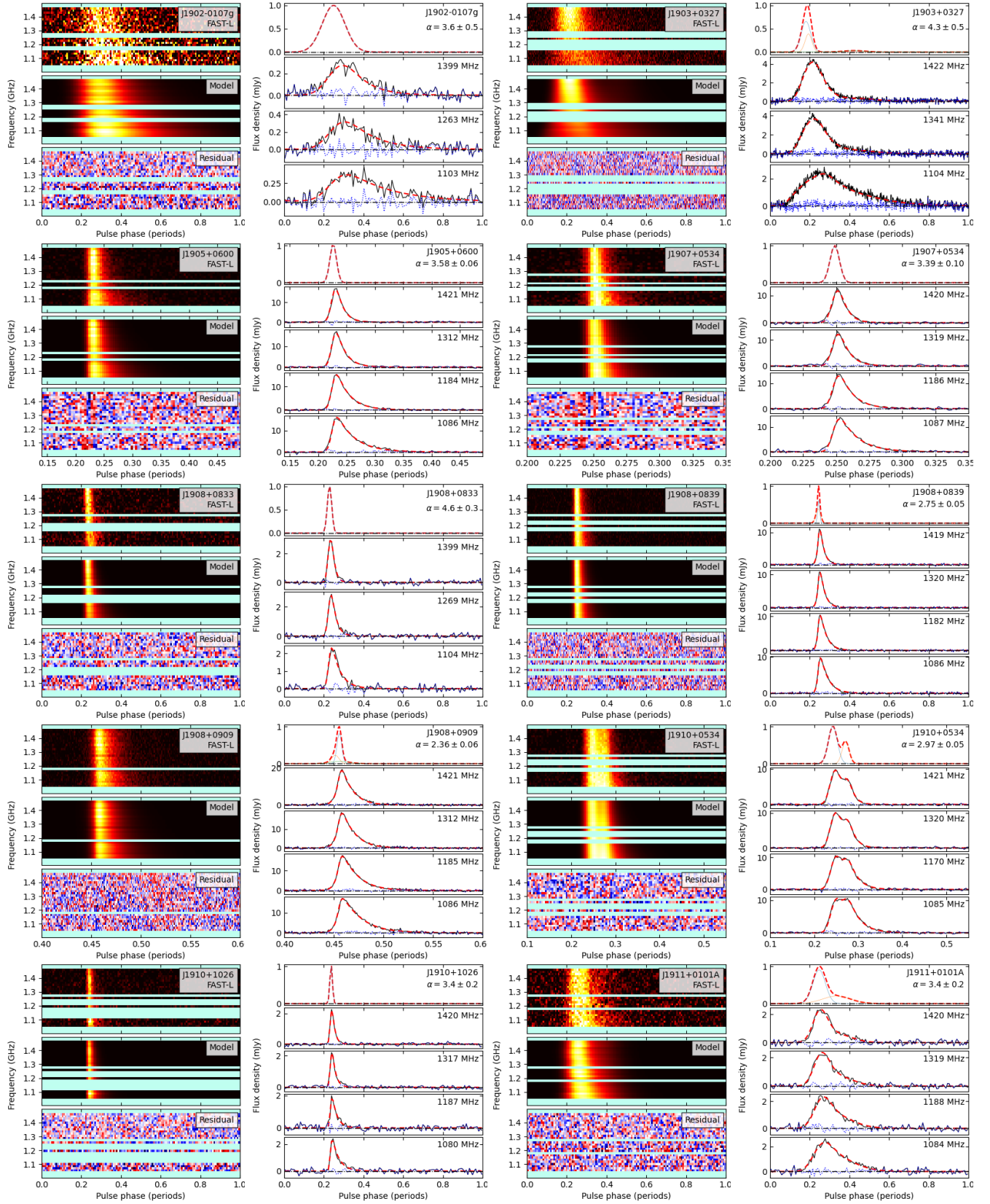


Figure A 1: — to be continued.

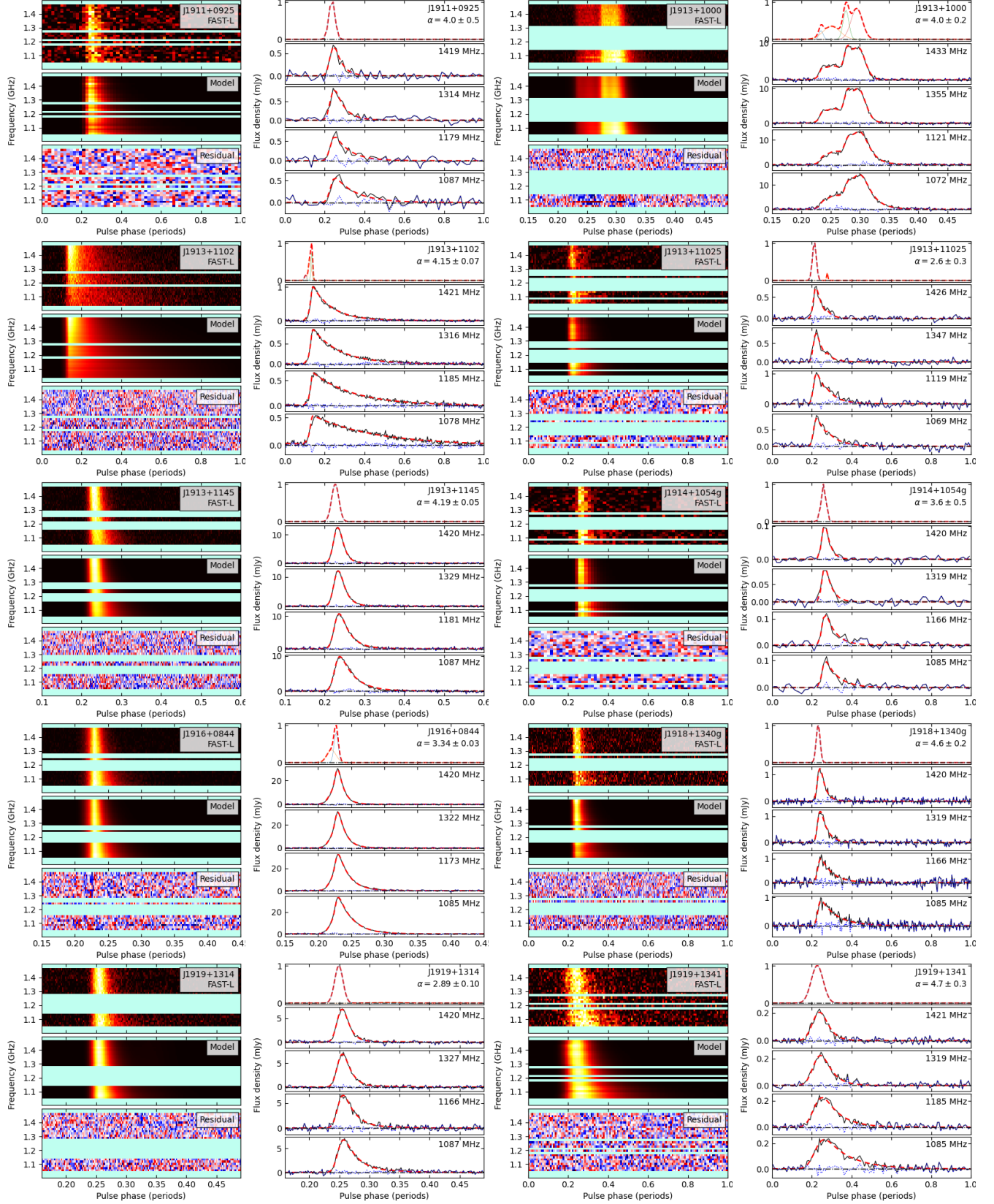


Figure A 1: — to be continued.

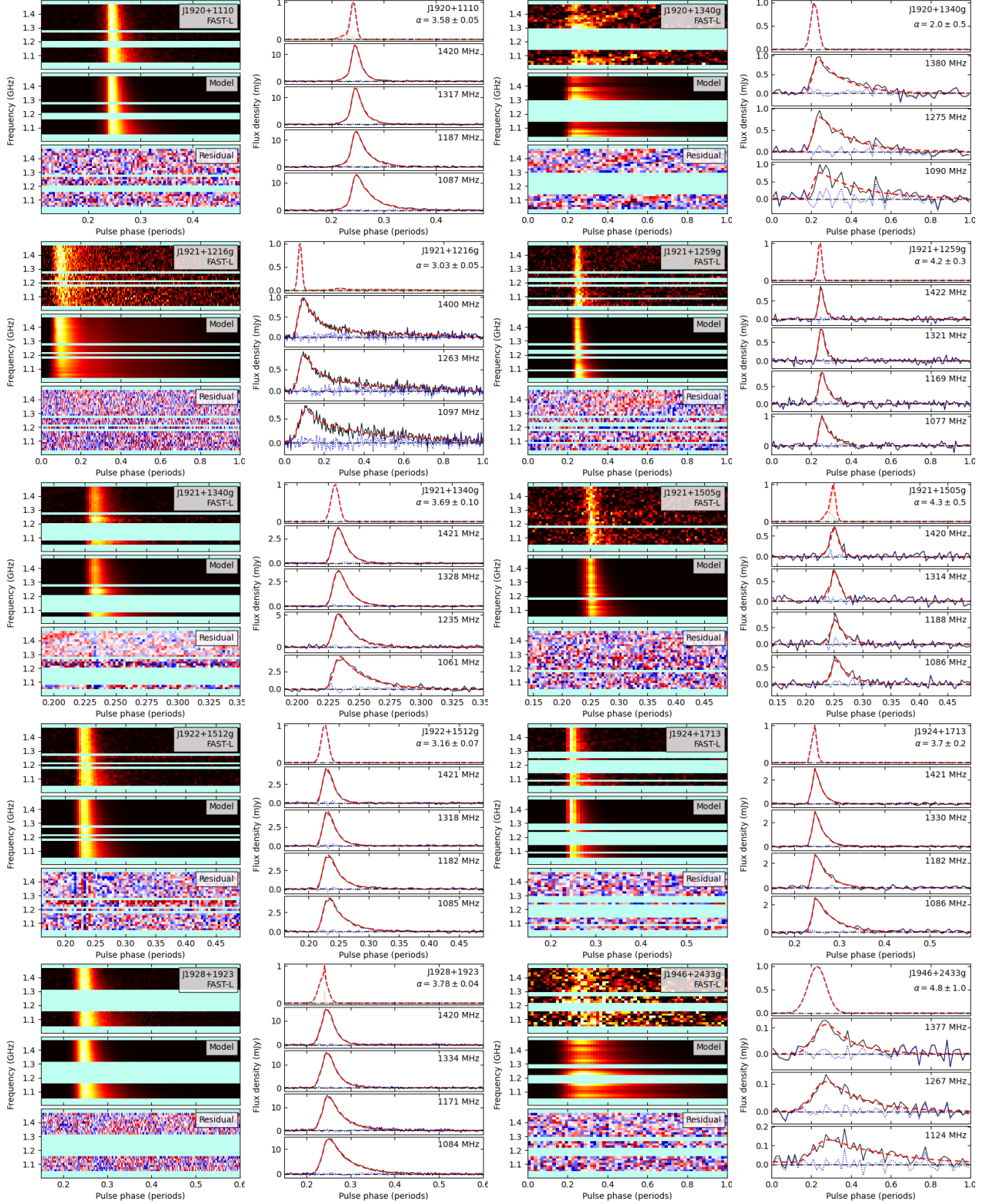


Figure A 1: — to be continued.

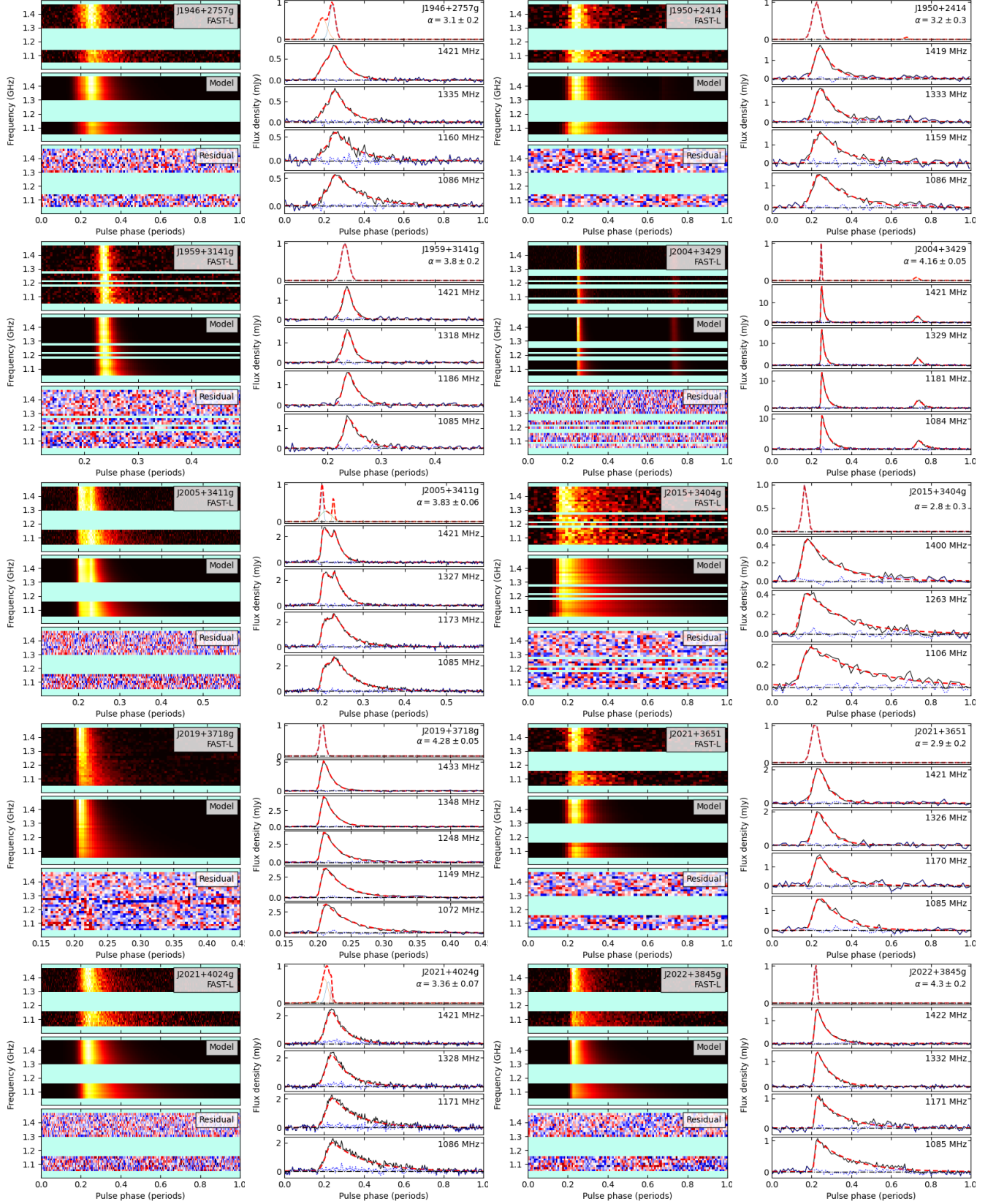


Figure A 1: — to be continued.

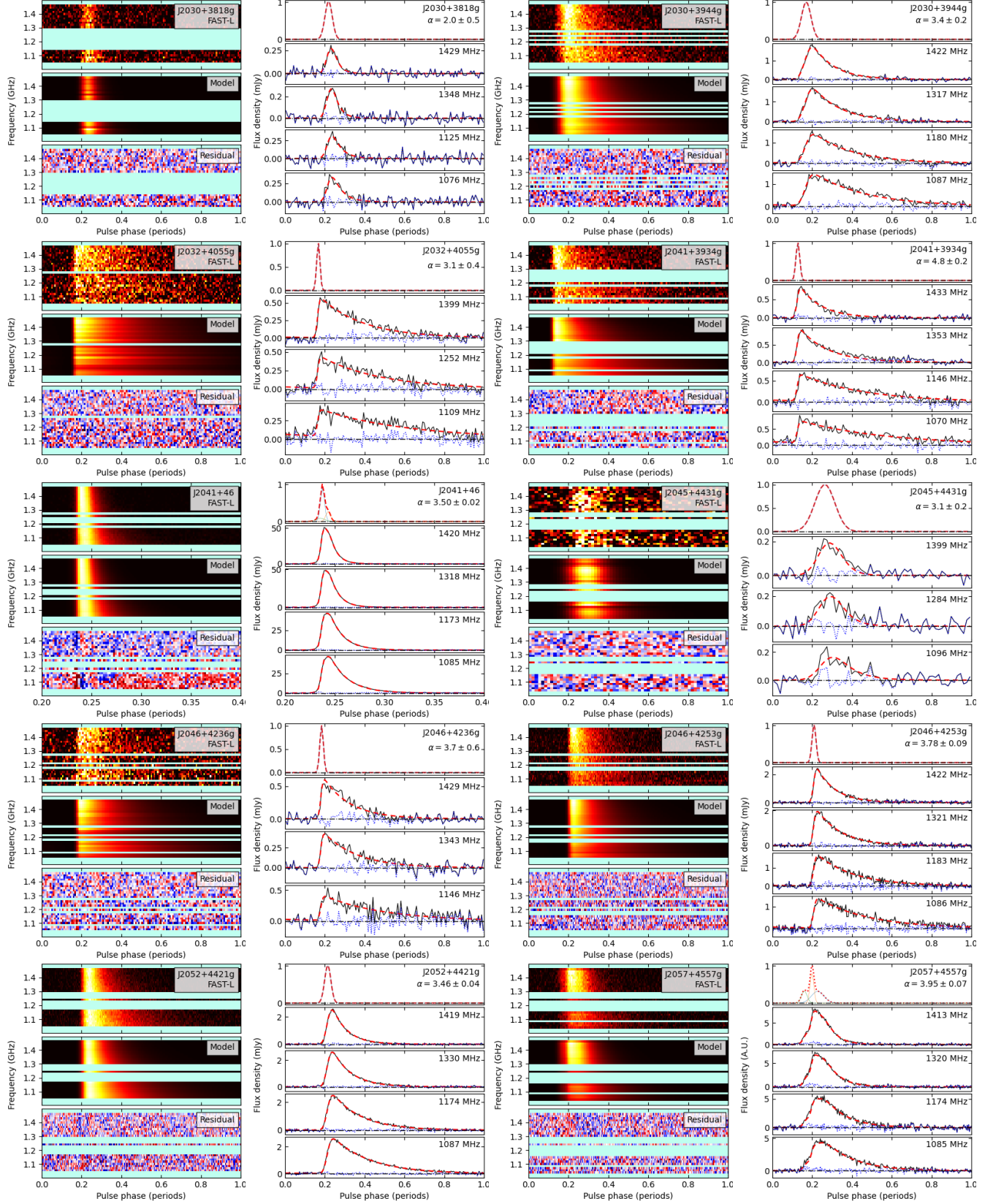


Figure A 1: — end.

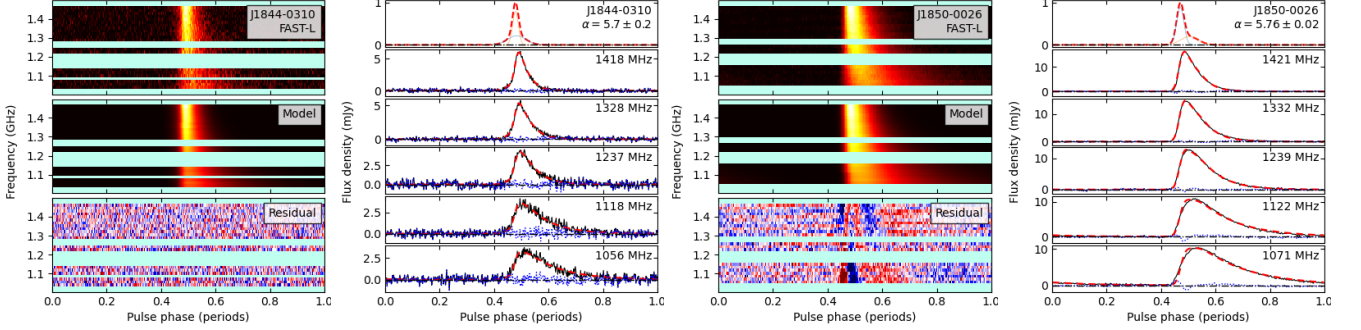


Figure A 2: The same as Figure 1 but for two unusual pulsars, PSR J1844-0310 and J1850-0026, which have to include the frequency-evolution for intrinsic profile components for the modeling, otherwise remarkable residuals will be left.

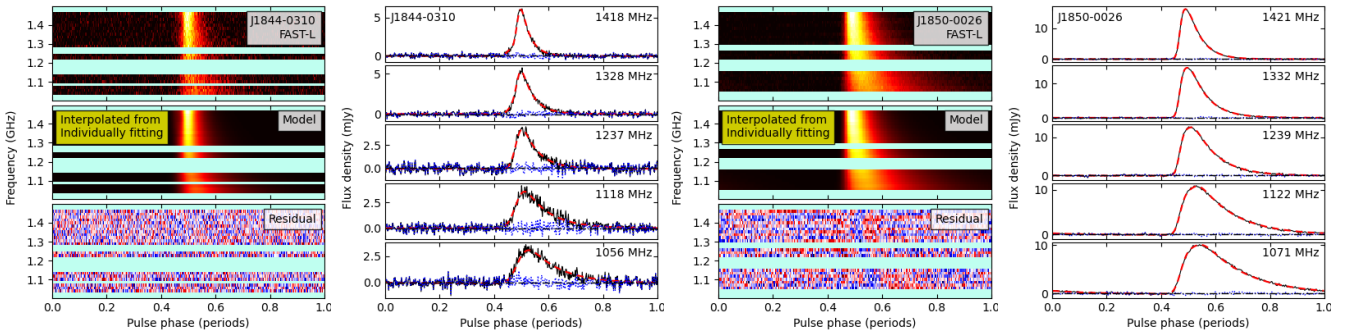


Figure A 3: The validation plot of two unusual pulsars, PSR J1844-0310 and J1850-0026, with the interpolated intrinsic profile from the individual fitting. Their residuals reach the noise level.

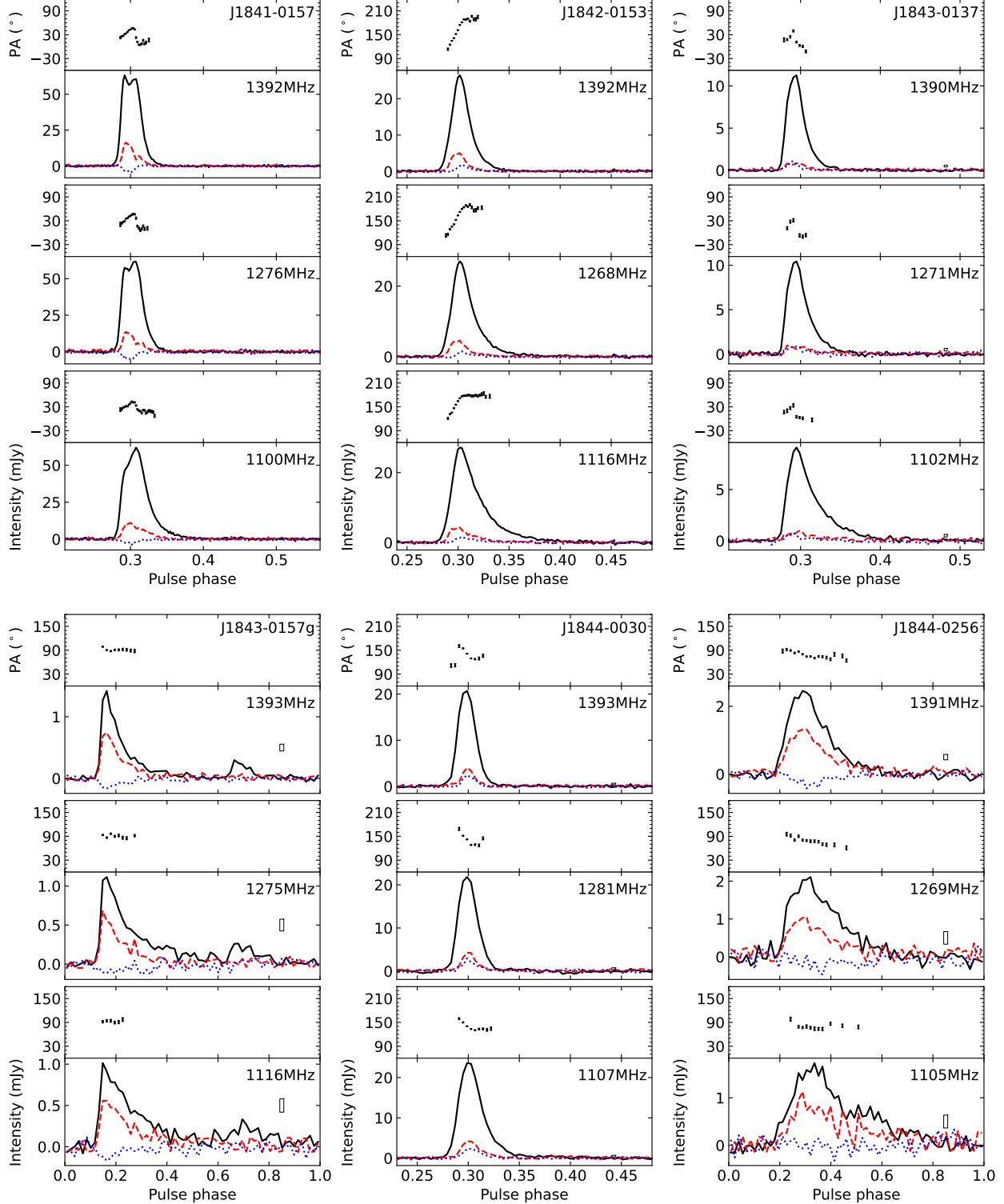


Figure A 4: Polarization profiles at 3 subbands of FAST observations for 41 scattered pulsars, including PSR J2052+4421 in Figure 1. Each profile has the total intensity in the solid line, linear polarization in the dashed line, and circular polarization in the dotted line. The band central frequency and the box for a bin size and $\pm 1\sigma$ are marked in the lower sub-panel. The polarization angles are plotted with error-bar in the upper sub-panel. – *to be continued.*

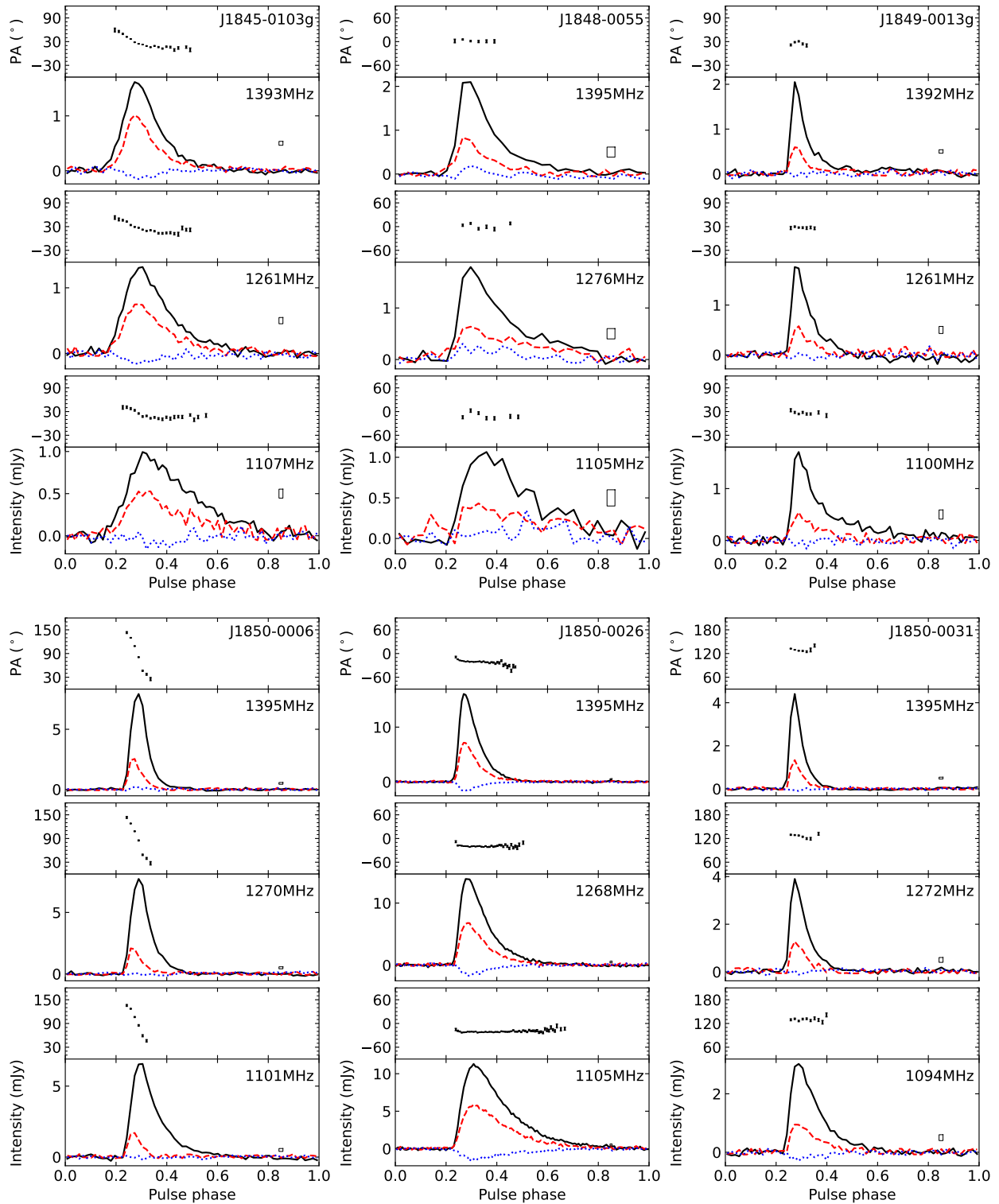
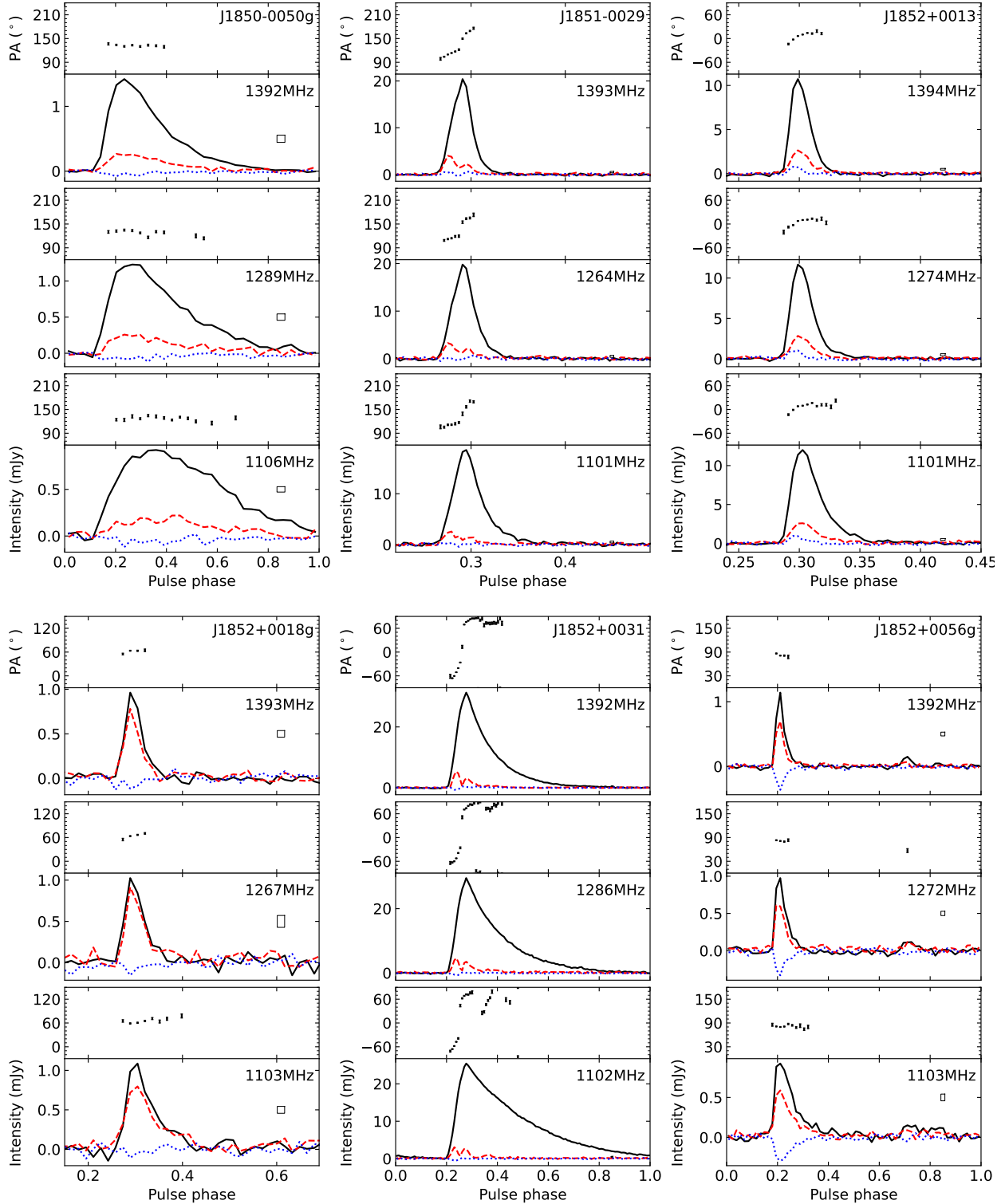


Figure A 4: – *continued*

**Figure A 4: – continued**

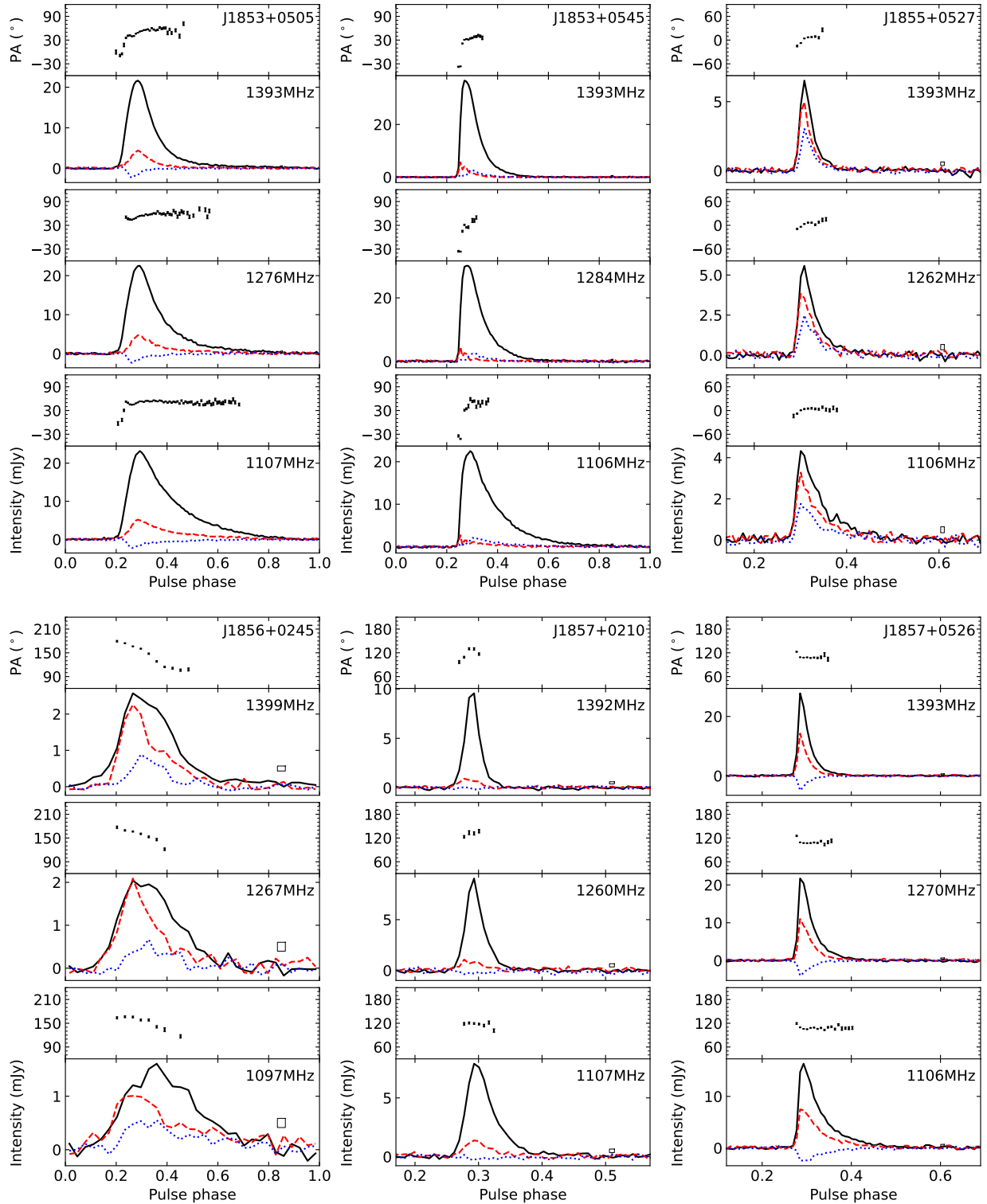
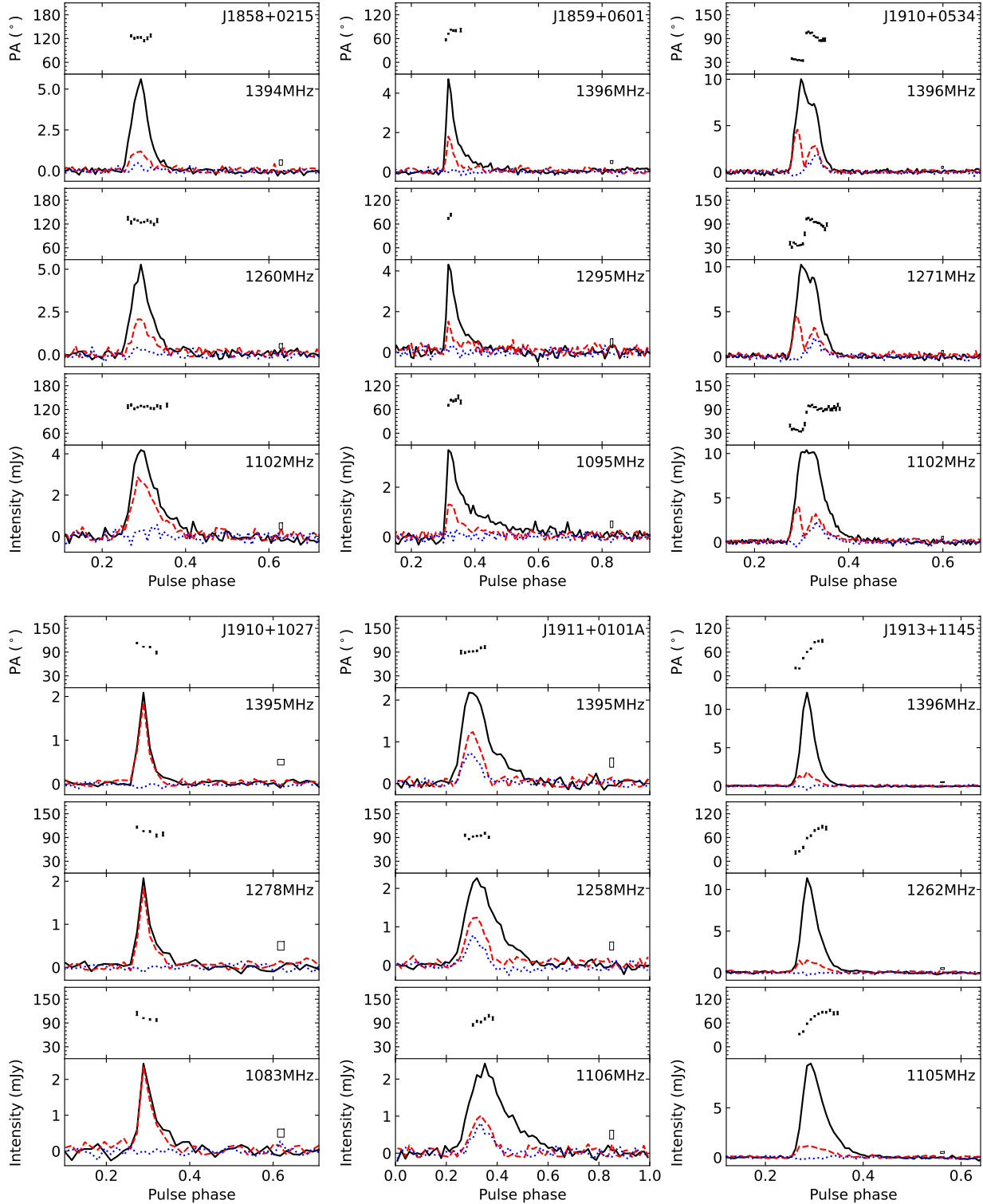
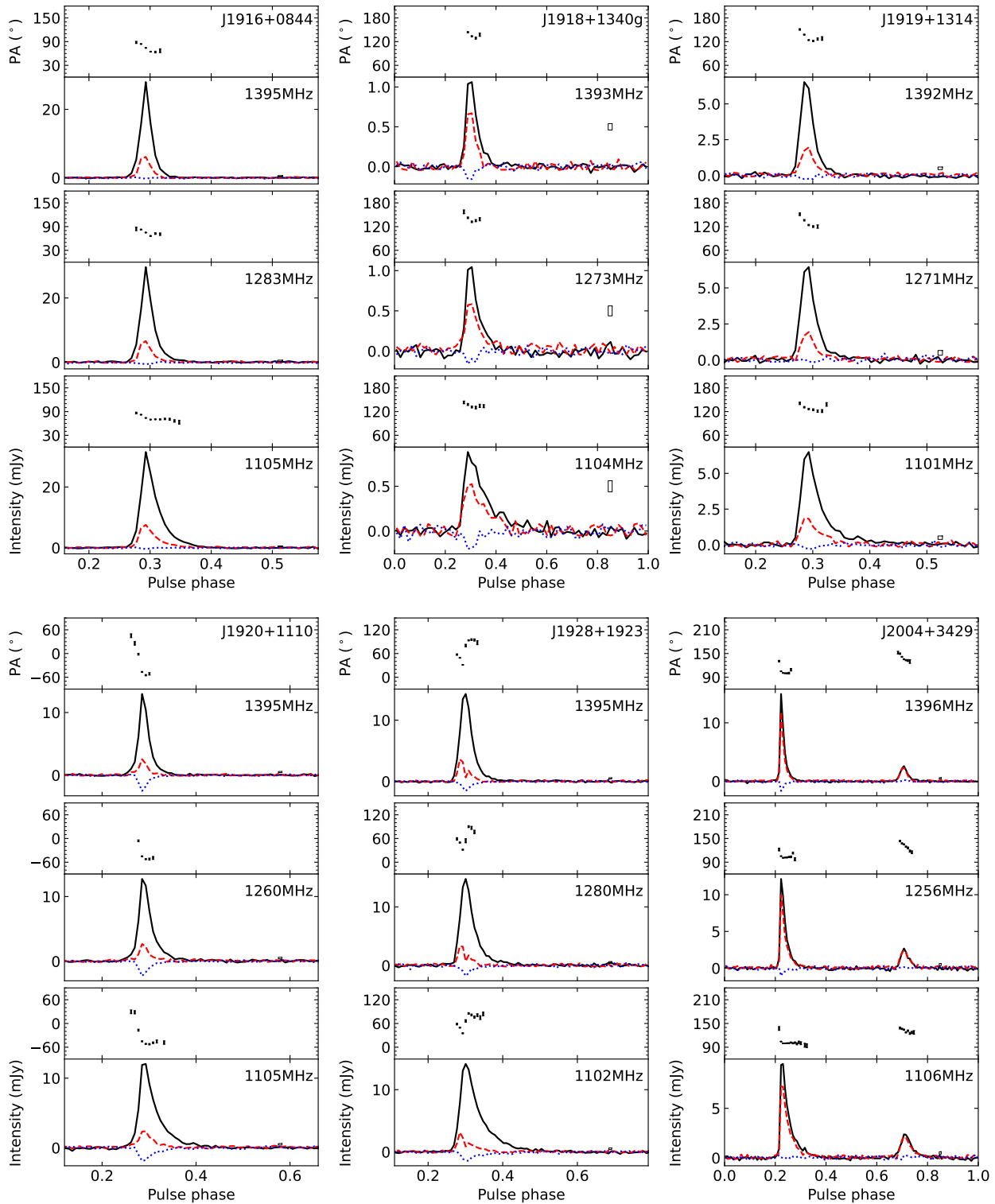


Figure A 4: – *continued*

**Figure A 4: – continued**

**Figure A 4:** – *continued*

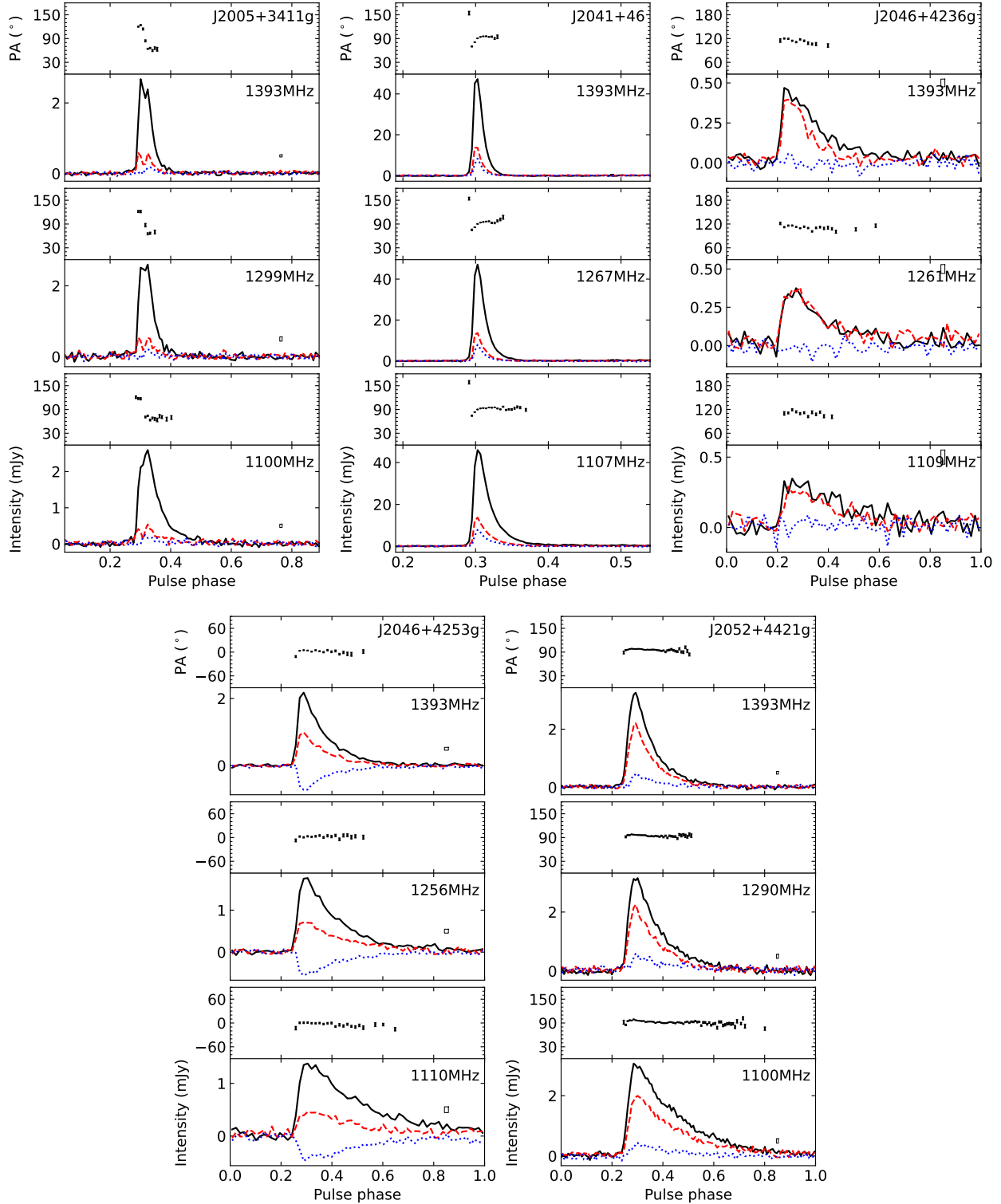
**Figure A 4:** – ended

Table A 2: Polarization parameters of subband profiles and the rotation measures for 41 scattered pulsars observed by FAST.

PSR Name	FAST Obs. Date yyyy-mm-dd	RM (rad/m ²)	<i>f</i> (MHz)	<i>I</i> (μJy)	<i>L/I</i> (%)	<i>V/I</i> (%)	$ V /I$ (%)
J1841-0157	2021-09-01	100.8 ± 0.4	1100	2414 ± 128	15.6 ± 3.0	-3.8 ± 3.0	3.2 ± 3.0
			1276	2070 ± 119	15.9 ± 3.0	-4.6 ± 3.0	4.1 ± 3.0
			1392	1957 ± 107	17.6 ± 3.0	-2.9 ± 3.0	3.5 ± 3.0
J1842-0153	2021-09-03	139.8 ± 0.5	1116	930 ± 50	12.9 ± 3.0	4.6 ± 3.0	4.5 ± 3.0
			1268	715 ± 41	14.2 ± 3.0	3.4 ± 3.0	3.5 ± 3.0
			1392	620 ± 34	16.6 ± 3.0	4.2 ± 3.0	4.0 ± 3.0
J1843-0137	2022-02-02	583 ± 2	1102	394 ± 23	10.4 ± 3.1	4.2 ± 3.0	5.1 ± 3.0
			1271	334 ± 24	10.5 ± 3.1	7.3 ± 3.1	7.5 ± 3.1
			1390	308 ± 21	8.7 ± 3.0	6.5 ± 3.0	6.6 ± 3.0
J1843-0157g	2021-09-03	230 ± 2	1116	172 ± 13	48.1 ± 4.6	-10.0 ± 3.6	5.6 ± 3.6
			1275	165 ± 12	40.1 ± 4.0	-11.0 ± 3.5	11.3 ± 3.5
			1393	147 ± 10	48.8 ± 3.7	-10.1 ± 3.3	10.2 ± 3.3
J1844-0030	2020-12-19	222.5 ± 0.7	1107	711 ± 41	14.9 ± 3.1	6.5 ± 3.0	7.4 ± 3.0
			1281	508 ± 49	15.1 ± 3.1	9.8 ± 3.0	9.3 ± 3.0
			1393	449 ± 34	13.9 ± 3.0	8.0 ± 3.0	7.6 ± 3.0
J1844-0256	2022-11-20	247 ± 3	1105	436 ± 27	50.3 ± 4.4	-2.0 ± 3.7	0.8 ± 3.7
			1269	428 ± 31	42.0 ± 3.8	-11.9 ± 3.5	9.1 ± 3.5
			1391	434 ± 24	53.0 ± 3.5	-10.8 ± 3.2	10.6 ± 3.2
J1845-0103g	2021-11-11	-1032.4 ± 0.7	1107	280 ± 15	48.3 ± 3.6	-6.9 ± 3.3	5.2 ± 3.3
			1261	274 ± 14	54.0 ± 3.3	-10.9 ± 3.2	8.6 ± 3.2
			1393	275 ± 14	54.9 ± 3.2	-4.6 ± 3.1	5.9 ± 3.1
J1848-0055	2021-10-24	-427 ± 7	1105	317 ± 22	39.9 ± 4.7	14.2 ± 4.1	9.5 ± 4.1
			1276	399 ± 25	43.8 ± 4.0	12.7 ± 3.5	11.3 ± 3.5
			1395	340 ± 28	33.7 ± 3.6	2.6 ± 3.1	5.6 ± 3.1
J1849-0013g	2023-09-16	-104 ± 2	1100	228 ± 16	26.6 ± 3.6	-2.1 ± 3.3	2.5 ± 3.3
			1261	153 ± 15	29.6 ± 3.6	-4.0 ± 3.3	1.5 ± 3.3
			1392	174 ± 9	29.7 ± 3.7	1.8 ± 3.4	1.7 ± 3.4
J1850-0006	2020-08-21	685.5 ± 0.6	1101	827 ± 43	14.5 ± 3.1	-1.4 ± 3.0	1.2 ± 3.0
			1270	712 ± 38	20.1 ± 3.1	-0.8 ± 3.0	0.9 ± 3.0
			1395	618 ± 33	26.1 ± 3.1	1.8 ± 3.0	1.7 ± 3.0
J1850-0026	2020-08-19	663.7 ± 0.2	1105	2368 ± 118	51.5 ± 3.0	-12.9 ± 3.0	12.6 ± 3.0
			1268	1852 ± 93	45.9 ± 3.0	-10.1 ± 3.0	10.0 ± 3.0
			1395	1466 ± 73	44.0 ± 3.0	-9.9 ± 3.0	9.7 ± 3.0
J1850-0031	2020-04-02	-206.3 ± 0.8	1094	396 ± 24	30.3 ± 3.3	-7.8 ± 3.1	6.2 ± 3.1
			1272	301 ± 24	30.8 ± 3.3	0.8 ± 3.1	1.3 ± 3.1
			1395	260 ± 15	29.5 ± 3.1	-2.1 ± 3.0	1.4 ± 3.0
J1850-0050g	2021-09-03	595 ± 5	1106	438 ± 22	17.7 ± 3.2	-7.4 ± 3.1	5.1 ± 3.1
			1289	414 ± 21	19.2 ± 3.2	-7.1 ± 3.1	5.2 ± 3.1
			1392	354 ± 19	19.4 ± 3.1	-4.1 ± 3.0	3.4 ± 3.0
J1851-0029	2021-03-06	649 ± 1	1101	723 ± 39	11.5 ± 3.1	0.1 ± 3.0	0.8 ± 3.0
			1264	583 ± 40	16.0 ± 3.1	1.0 ± 3.0	2.1 ± 3.0
			1393	524 ± 33	16.9 ± 3.0	2.3 ± 3.0	2.5 ± 3.0
J1852+0013	2020-08-26	462.6 ± 0.6	1101	357 ± 23	20.3 ± 3.1	3.3 ± 3.0	4.9 ± 3.0
			1274	318 ± 19	24.4 ± 3.2	1.9 ± 3.2	5.4 ± 3.2
			1394	211 ± 17	24.7 ± 3.1	4.4 ± 3.0	5.5 ± 3.0
J1852+0018g	2020-09-15	72 ± 2	1103	78 ± 9	77.3 ± 4.5	-3.2 ± 3.7	2.3 ± 3.7
			1267	53 ± 18	77.7 ± 5.8	-10.3 ± 3.7	6.1 ± 3.7
			1393	43 ± 9	71.7 ± 4.7	-9.4 ± 3.8	4.2 ± 3.7
J1852+0031	2021-11-14	315.0 ± 0.4	1102	7064 ± 353	4.5 ± 3.0	0.2 ± 3.0	0.4 ± 3.0
			1286	5511 ± 275	8.0 ± 3.0	-0.8 ± 3.0	0.7 ± 3.0
			1392	4701 ± 235	7.5 ± 3.0	0.5 ± 3.0	1.2 ± 3.0
J1852+0056g	2021-02-07	-90.5 ± 0.9	1103	102 ± 7	54.4 ± 3.7	-22.0 ± 3.3	22.2 ± 3.3
			1272	54 ± 6	62.0 ± 4.1	-31.8 ± 3.5	29.7 ± 3.5
			1392	50 ± 6	58.7 ± 4.0	-27.5 ± 3.4	27.1 ± 3.4

... to be continued.

Table A 2: – *continued*

PSR Name	FAST Obs. Date yyyy-mm-dd	RM (rad/m ²)	<i>f</i> (MHz)	<i>I</i> (μJy)	<i>L/I</i> (%)	<i>V/I</i> (%)	$ V /I$ (%)
J1853+0505	2021-04-22	11.1 ± 0.3	1107	4823 ± 241	20.1 ± 3.0	-5.8 ± 3.0	5.7 ± 3.0
			1276	3672 ± 184	18.8 ± 3.0	-4.2 ± 3.0	5.0 ± 3.0
			1393	2911 ± 145	16.9 ± 3.0	-3.0 ± 3.0	4.9 ± 3.0
J1853+0545	2020-08-01	78.0 ± 0.6	1106	3440 ± 172	5.4 ± 3.0	9.1 ± 3.0	8.8 ± 3.0
			1284	3133 ± 157	5.8 ± 3.0	6.5 ± 3.0	6.3 ± 3.0
			1393	3067 ± 153	8.0 ± 3.0	6.2 ± 3.0	6.1 ± 3.0
J1855+0527	2020-04-19	124.6 ± 0.6	1106	281 ± 23	64.0 ± 3.9	37.0 ± 3.5	33.3 ± 3.5
			1262	246 ± 29	66.9 ± 3.7	40.3 ± 3.4	40.9 ± 3.4
			1393	219 ± 26	70.5 ± 3.5	41.5 ± 3.3	40.3 ± 3.3
J1856+0245	2020-11-04	269.3 ± 0.9	1097	499 ± 28	62.1 ± 4.3	31.1 ± 3.3	31.0 ± 3.3
			1267	531 ± 32	67.0 ± 4.3	18.2 ± 3.5	17.9 ± 3.5
			1399	631 ± 33	63.3 ± 3.6	20.4 ± 3.1	21.9 ± 3.1
J1857+0210	2021-01-26	105 ± 3	1107	408 ± 31	16.5 ± 3.2	-3.4 ± 3.1	2.7 ± 3.1
			1260	308 ± 32	12.3 ± 3.4	-5.4 ± 3.2	4.4 ± 3.2
			1392	282 ± 24	11.5 ± 3.1	-0.6 ± 3.0	1.0 ± 3.0
J1857+0526	2020-05-14	959.4 ± 0.3	1106	989 ± 55	46.5 ± 3.1	-15.9 ± 3.1	15.3 ± 3.1
			1270	864 ± 52	45.6 ± 3.1	-15.2 ± 3.0	14.1 ± 3.0
			1393	844 ± 51	45.0 ± 3.1	-15.0 ± 3.0	15.1 ± 3.0
J1858+0215	2020-04-18	-2.6 ± 1.3	1102	313 ± 26	59.8 ± 3.9	5.0 ± 3.4	4.2 ± 3.4
			1260	293 ± 24	35.7 ± 3.6	2.4 ± 3.4	4.5 ± 3.4
			1394	257 ± 32	23.7 ± 3.3	5.2 ± 3.2	3.0 ± 3.2
J1859+0601	2020-08-21	76.3 ± 0.4	1095	300 ± 20	30.4 ± 3.8	5.2 ± 3.4	2.4 ± 3.4
			1295	197 ± 27	31.3 ± 4.5	1.9 ± 3.8	4.1 ± 3.8
			1396	215 ± 13	30.7 ± 3.5	2.1 ± 3.3	1.8 ± 3.3
J1910+0534	2021-06-21	349.8 ± 0.4	1102	723 ± 39	30.1 ± 3.0	11.3 ± 3.0	12.6 ± 3.0
			1271	554 ± 33	34.5 ± 3.1	9.6 ± 3.1	12.2 ± 3.1
			1396	492 ± 27	34.7 ± 3.1	8.7 ± 3.0	12.7 ± 3.0
J1910+1027	2020-11-23	207.3 ± 0.9	1083	115 ± 25	74.9 ± 6.3	-4.2 ± 4.5	-4.2 ± 4.5
			1278	79 ± 27	75.1 ± 5.2	0.0 ± 3.7	0.5 ± 3.7
			1395	65 ± 19	85.3 ± 4.5	-6.8 ± 3.7	4.1 ± 3.7
J1911+0101A	2020-12-02	124.7 ± 1.3	1106	389 ± 25	23.1 ± 3.7	17.1 ± 3.4	14.8 ± 3.4
			1258	321 ± 22	39.0 ± 3.5	13.0 ± 3.3	19.4 ± 3.4
			1395	294 ± 22	35.4 ± 3.7	21.9 ± 3.2	19.6 ± 3.2
J1913+1145	2020-05-23	921.9 ± 0.9	1105	530 ± 29	15.4 ± 3.1	-0.6 ± 3.0	1.6 ± 3.0
			1262	460 ± 28	17.8 ± 3.1	-1.2 ± 3.0	0.4 ± 3.0
			1396	409 ± 23	16.1 ± 3.0	-1.3 ± 3.0	2.5 ± 3.0
J1916+0844	2020-12-15	601.0 ± 0.4	1105	1057 ± 54	24.9 ± 3.0	-0.7 ± 3.0	0.7 ± 3.0
			1283	740 ± 48	22.8 ± 3.1	-1.9 ± 3.0	1.5 ± 3.0
			1395	602 ± 40	23.2 ± 3.0	-0.4 ± 3.0	0.7 ± 3.0
J1918+1340g	2020-08-07	740 ± 2	1104	78 ± 13	61.5 ± 5.0	-15.9 ± 3.8	11.3 ± 3.7
			1273	62 ± 14	59.5 ± 4.8	-10.2 ± 3.9	8.0 ± 3.9
			1393	57 ± 10	54.6 ± 4.5	-10.8 ± 3.5	11.0 ± 3.5
J1919+1314	2021-10-12	1981 ± 1	1101	277 ± 22	27.9 ± 3.5	-2.2 ± 3.2	1.7 ± 3.2
			1271	212 ± 33	28.9 ± 3.5	-1.4 ± 3.2	1.4 ± 3.2
			1392	192 ± 19	28.6 ± 3.2	-3.7 ± 3.1	4.1 ± 3.1
J1920+1110	2020-05-09	653.9 ± 0.9	1105	568 ± 32	16.6 ± 3.1	-12.1 ± 3.1	11.9 ± 3.1
			1260	462 ± 28	18.5 ± 3.2	-12.3 ± 3.1	12.0 ± 3.1
			1395	362 ± 23	17.3 ± 3.1	-15.6 ± 3.1	14.8 ± 3.1
J1928+1923	2020-08-04	344.8 ± 0.6	1102	919 ± 48	12.2 ± 3.0	-9.0 ± 3.0	8.7 ± 3.0
			1280	704 ± 41	15.0 ± 3.2	-9.1 ± 3.1	6.9 ± 3.1
			1395	599 ± 32	17.7 ± 3.1	-7.5 ± 3.0	7.9 ± 3.0
J2004+3429	2020-04-19	158.7 ± 0.3	1106	529 ± 29	76.8 ± 3.2	3.7 ± 3.1	2.4 ± 3.1
			1256	422 ± 29	82.5 ± 3.3	-4.2 ± 3.2	3.7 ± 3.2
			1396	386 ± 25	76.4 ± 3.2	-8.3 ± 3.1	9.0 ± 3.1

... to be continued.

Table A 2: – *continued*